Insights into self-discharge of lithium and magnesium sulfur batteries

Raphael Richter,[†,‡] Joachim Häcker,[†] Zhirong Zhao-Karger,[¶] Timo Danner,[†,‡] Norbert Wagner,[†] Maximilian Fichtner,[‡,¶] K. Andreas Friedrich,[†,§] and Arnulf Latz[*,†,‡,‖]

†*Institute of Engineering Thermodynamics, German Aerospace Center (DLR), Pfaffenwaldring 38-40, 70569 Stuttgart, Germany*

‡*Helmholtz Institute Ulm (HIU), Helmholtzstrasse 11, 89081 Ulm, Germany*

¶*Institute of Nanotechnology, Karlsruhe Institute of Technology (KIT), P.O. Box 3640, 76021 Karlsruhe, Germany*

§*Institute of Energy Storage, University of Stuttgart, Pfaffenwaldring 31, 70569 Stuttgart, Germany*

‖*Institute of Electrochemistry, University of Ulm, Albert-Einstein-Allee 47, 89081 Ulm, Germany*

E-mail: arnulf.latz@dlr.de

Abstract

Magnesium-sulfur (Mg-S) batteries represent a very promising emerging cell chemistry. However, developments in Mg-S batteries are in an early stage, and the system exhibits problems similar to those of early lithium-sulfur batteries (Li-S). The significant challenges are the low coulombic efficiency and short cycle life of Mg-S batteries, mainly associated with the well-known polysulfide shuttle. An obvious result of this phenomenon is the rapid self-discharge of Mg-S batteries. In this article, we present a

multiscale simulation framework for metal-sulfur batteries. In our approach, we provide a continuum description of chemical and electrochemical processes at the positive and negative electrodes. In combination with a 1D model for the transport of dissolved species in the electrolyte, this approach allows us to reproduce and interpret experimental data measured on Li-S and Mg-S batteries. We focus on the common properties of Li-S and Mg-S batteries as well as on the key differences causing the much more rapid self-discharge of the Mg system. We identify side reactions on the anode surface as a limiting process, while other factors, such as the mobility of dissolved species and solid phase kinetics, play a minor role.

Keywords

Lithium-sulfur battery, Magnesium-sulfur battery, Modeling, Meso/micro-porous carbon, Self-discharge

1 Introduction

The expected increase of electric vehicles in the transportation sector amplifies the demand for energy storage technology with a high energy density. For almost a decade, lithium-sulfur batteries (Li-S) have been discussed as a promising next-generation battery technology.[1,2] Compared to Li-Ion batteries, the Li-S system is based on the conversion of active materials instead of the intercalation of lithium ions in the active material. The high theoretical capacity of sulfur of 1672 mAh g^{-1} in combination with a lithium-metal electrode results in a theoretical energy density of 2800 Wh l^{-1} based on the complete conversion to Li_2S.[3] Furthermore, the abundance and low cost of sulfur makes the system attractive for large-scale application. Large-scale production of Li-S batteries cannot be established yet. The main challenges for the large-scale production of Li-S batteries are the low coulombic efficiency and cycle life of the battery, which are associated with the polysulfide shuttle. Dissolved

polysulfides can diffuse to the anode, which leads to parasitic charge transport within the cell. This so-called "shuttle effect" reduces the capacity and coulombic efficiency of the cells. To avoid these problems, numerous approaches have been suggested in the literature and are summarized in several review articles.[4–7] Furthermore, the multistep reduction and oxidation reaction mechanism of dissolved polysulfides, as well as the phase-change behavior due to the dissolution and precipitation of elemental sulfur and lithium sulfide, is still not fully understood.[8,9] Moreover, the stability of the Li metal electrode and the availability of lithium in the long term are a general matter of debate.[10]

These issues give rise to increasing interest in alternatives to lithium metal. Among other metals, magnesium is seen as one of the most promising candidates. Magnesium is an abundant element that is commercially available in large quantities and at a relatively low cost, and additionally, Mg shows no dendrite formation during plating and stripping.[11,12] Moreover, Mg allows the storage of two electrons per atom, which compensates for its generally lower cell voltage. In combination with sulfur as the positive electrode material, the theoretical open-circuit voltage is 1.7 V, and the theoretical energy density is as high as 3200 Wh l^{-1}, based on a two-electron conversion reaction expressed as $S^{2-} + Mg^{2+} \rightleftharpoons MgS$.[3] This energy density is greater than that of Li-S batteries, and therefore, Mg is very promising for mobile device and automotive applications.

The operation of Mg-ion batteries was first demonstrated by Aurbach and his group around 2000.[13] The electrolytes are used in this study show reversible Mg deposition and stripping but, due to their nucleophilic nature, they are not compatible with sulfur electrodes. The first non-nucleophilic electrolyte for Mg batteries was developed in 2011 by Kim et al.[14] and led to the rapid development of further alternative electrolytes.[15–17] These electrolytes provide the opportunity to use sulfur as the positive electrode material. Note that the same electrolyte systems can, in principle, also be used in Mg-ion batteries. The first Mg-S batteries exhibited problems similar to those of Li-S batteries, including a low coulombic efficiency and cycle life, but the effects were much more pronounced. Most of the issues are

probably also associated with the shuttle of polysulfides between the electrodes. Moreover, the reactions at both the positive and the negative electrode are even less understood. In the literature, similar sulfur reduction mechanisms in Li-S and Mg-S batteries are generally assumed.[3,16–22]

Mg batteries are in an early stage of research, and certainly, a variety of additional fundamental questions need to be answered. To reduce the development time, conceptual similarities to Li-based systems should be exploited, and models on the continuum scale provide a tool to investigate the influence of the physical and chemical properties of the electrodes and electrolyte on cell behavior. In contrast to the plentiful experimental literature on metal-sulfur (Me-S) batteries, especially on Li-S batteries, the literature on mathematical models of Me-S batteries is surprisingly small.

The first continuum models of Li-S batteries were developed by Mikhaylik et al.,[23] including a simple shuttle effect. Kumaresan et al.[24] presented a detailed model describing the complex reduction mechanism of sulfur using a multispecies transport formulation. The same model was used by et al.[25–27] for intensive parameter studies. Fronczek et al.[28] presented an enhanced model allowing the simulation of the battery charge and electrochemical impedance spectra. Due to the uncertainty of the kinetic mechanisms in Li-S batteries, Hofmann et al.[29] reduced the number of reaction intermediates during sulfur reduction to study the polysulfide shuttle. This reduced model was capable of representing the key characteristics of a Li-S battery and its discharge behavior. Zhang et al.[30] developed a model to qualitatively study the change of electrolyte resistance during cell operation. Danner et al.[31] presented a 1+1D model addressing the benefits of nanostructured sulfur-carbon cathodes on battery performance and cycling stability. This approach was extended by Thangavel et al.[32] by considering the exchange of species between the macroscopic domain and microporous particles. Thereby, they were able to describe the evolution of the species concentration during discharge within the hierarchical pore network of the positive electrode. Furthermore, they studied the effects of different cathode parameters, such as sulfur loading, particle size, pore

size and pore size distribution, on the capacity or evolution of porosity. In a simplified approach, Yin et al. studied the mechanism of ultra-microporous carbons in quasi-solid-state Li-S batteries.[33]

To the best of our knowledge, there is only one continuum model[34] published in the literature describing Mg plating and stripping at the Mg metal anode. Continuum models of full battery cells, especially Mg-S cells, have not yet been published. To take advantage of the conceptual similarities between Li-S and Mg-S batteries, we formulate a common framework for metal-sulfur batteries (Me-S). In a multiscale approach, we describe the processes both in sulfur host materials (e.g., meso/microporous carbons) and at the cell level (1+1D), which intrinsically provides a description of the polysulfide shuttle. By considering side reactions at the negative electrode, the model can reproduce the self-discharge of Me-S batteries after cell assembly.

This article is structured as follows. First, we describe the setup of our model experiments on Li-S and Mg-S cells. Measurements are performed on geometrically similar cells with the same sulfur-carbon composite cathodes and the same solvent system. In the next section, we provide a derivation and description of our system of constitutive equations implemented within our simulation framework for Me-S batteries. The results of the simulations, as well as the corresponding experimental data, are presented in Section 4. After validation of the model parameterization in Section 4.1, we present a comprehensive simulation study investigating the influence of kinetic and thermodynamic parameters on the self-discharge of Me-S batteries. The simulation results provide insights into the qualitative differences between the Li-S and Mg-S systems and directions for research on improved materials for Mg-S batteries.

2 Experimental

In this section, the details of the electrode preparation, cell assembly and electrochemical characterization of Li-S and Mg-S battery cells are provided. Individual cells are prepared in

the same Swagelok-type setup with the same positive electrode and separator to eliminate geometrical deviations between the Li-S and Mg-S systems. Moreover, we use the same solvent system consisting of a mixture of TEGDME:DEGDME. Commonly, additives such as $LiNO_3$ are added to Li-S batteries to increase their cycling stability and reduce the polysulfide shuttle.[35] Similar additives could not be identified for Mg-S batteries. Therefore, we do not use additional additives in either system to focus on the differences between Mg-S and Li-S cell chemistry.

2.1 Sulfur composite cathode

Positive sulfur composite electrodes are prepared by the widely used melt infiltration method. Therefore, sulfur (99.5 %, Alfa Aesar) and Ketjenblack EC-600 JD (Akzo Nobel) are ball-milled in a mass ratio of 5:4 for 15 min at 500 rpm. After the procedure, the powder is transferred to an argon-filled glovebox (Jacomex GPT4FF, <1 ppm H_2O, <3 ppm O_2) and filled in a glass vessel. The vessel is placed inside a stainless-steel autoclave and infiltrated for 20 h at 155 °C with a heating rate of 0.5 K min^{-1}. To remove excess sulfur from the surface of the porous carbon matrix, the powder is subsequently filled in a customized glass vessel under an argon atmosphere, transferred to a glass tube furnace and further heated at 300 °C for 1 h. A polyvinylidene fluoride (PVDF) solution (4 wt. % Solvay Solef 5130 in dimethyl sulfoxide, DMSO) and DMSO (VWR ProLab Chemicals) are added to the S/C powder, and the slurry is stirred for 2 h at 500 rpm to obtain a homogeneous dispersion. Subsequently, the slurry is doctor-bladed on a carbon-coated aluminum foil and dried for 12 h at 60 °C. In the final step, the electrodes are dried for 1 h under vacuum. The resulting thickness of the cathode layers is 40 µm. By thermogravimetric analysis (TGA), we obtain a cathode composition of 48 wt.% sulfur, 42 wt.% carbon and 10 wt.% PVDF, which corresponds to a sulfur loading of approximately 0.75 mg cm^{-2}.

2.2 Metal anode

A lithium metal foil (99.9 %, 750 μm, Alfa Aesar) and magnesium metal foil (99.9 %, 250 μm, Goodfellow) of 18 mm in diameter are used as negative electrodes in Li-S and Mg-S cells, respectively. To remove the oxide layer on its surface, the magnesium anode is scraped mechanically prior to cell assembly.

2.3 Electrolyte

Electrolyte preparation is performed in an argon-filled glovebox. The vessels are dried in a vacuum furnace to remove surface water molecules. The electrolyte solution in Li-S cells comprises 1 M LiTFSI (99.95 %, Sigma-Aldrich) in a 1:1 vol. mixture of TEGDME (>99 %, Sigma-Aldrich) and DEGDME (anhydrous, 99.5 %, Sigma-Aldrich) and is prepared by stoichiometric mixing at 500 rpm for 24 h. The electrolyte of the Mg-S cells contains 1.4 M of $(HMDS)_2Mg\text{-}AlCl_3$ in 1:1 vol. TEGDME / DEGDME. For more details on the development, synthesis, and handling of the Mg salt, see Ref. 3. The concentrations of the electrolytes are chosen to be representative of typical values in the literature.

2.4 Cell assembly

Swagelok-type cells (∅ 22 mm) in a two-electrode setup are assembled under an argon atmosphere. A spring is included in the cell, and a defined load of 45 N is applied during cell assembly to guarantee a homogeneous pressure distribution. Because Mg-S cells still require a large excess electrolyte volume and perform best with glass fiber separators, the same separator (GF/C, ∅ 22 mm, thickness of 260 μm, 1.2 μm particle retention, Whatman) and a large electrolyte volume of 150 μL are used for both cell setups. Carbon-coated aluminum foil is added between the electrodes and current collectors to mitigate the corrosion of the stainless steel current collectors by the chloride species in the Mg-S electrolyte. All the cell components are dried for 12 hours under vacuum before use. The drying temperatures for

the separator and Swagelok parts are set to 100 °C and 60 °C, respectively.

2.5 Test procedure

For the investigation of the evolution of the open-circuit voltage (OCV) under open-circuit conditions (later referred to as OCV conditions), the cell is stored at room temperature for 1 h and 24 h, respectively. The subsequent discharge is performed at a rate of C/10 (167.2 mA g_S^{-1}). The lower cut-off voltage during discharge is set to 1.7 V for Li-S cells and 0.05 V for Mg-S cells, respectively. For the Mg-S cells, an additional experiment with a rest period of 5 h is performed to resolve the temporal evolution of the self-discharge.

3 Theory

For this study a common framework for the simulation of Me-S batteries was developed. Compared to our earlier work on Li-S batteries,[31] we generalize our implementation which allows us to specify various material and reaction parameters. Thereby, different cell chemistries can be simulated and compared within a single simulation tool. A detailed description of the governing equations and key assumptions is provided in the sections below. In this study, the first results demonstrating the methodology for Mg-S and Li-S batteries are presented.

3.1 Simulation domain

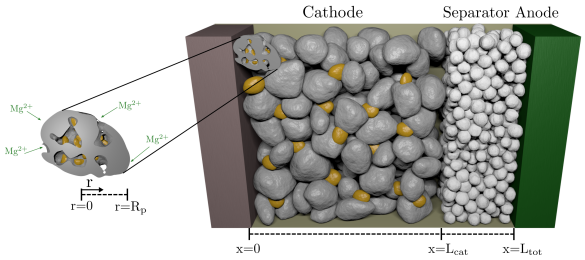

Figure 1: Schematic of a metal-sulfur cell in which sulfur is infiltrated into the porous carbon structure. The coordinates of the macroscopic modeling domain (cell) and the microscopic particle are denoted by x and r, respectively.

Typically, Me-S cells consist of a metal anode, porous separator, and porous carbon/sulfur composite cathode. The latter is made of carbon, a binder, and the active material. These constituent parts are either soaked in or at least in contact with the liquid electrolyte. A schematic illustration of the geometry is shown in Fig. 1. Our model resolves the distributions of species, solids and potential within the positive electrode and the separator domain. The different simulation domains have a finite thickness of L_{cat} and L_{sep}. The negative electrode is modeled as a metallic surface at the position $L_{\mathrm{tot}} = L_{\mathrm{cat}} - L_{\mathrm{sep}}$. Chemical and electrochemical reactions take place directly on the anode surface. To model these reactions, we introduce a small volume element directly on the anode surface, analogous to our previous studies.[29]

Several approaches are reported in the literature that aim for the retention of sulfur within the cathode domain.[36] As described in 2.1, we use the common melt infiltration technique to embed sulfur into a porous carbon structure providing electronic conductivity and improved cycling stability. The porous carbon particles lead to a bimodal pore size distribution. This distribution can be classified into: I) macropores between the carbon host particles and II) micropores due to the internal pore structure of the particles. To clearly distinguish between these scales, the macropores are, in the following, referred to as the cell scale, and the micropores are referred to as the particle scale.

The cell model (coordinate x) describing the transport of mass and charge between the cathode and anode is extended by a particle model (coordinate r) describing the reaction and transport of dissolved species within particles, as illustrated in Fig. 1. The particle model assumes a representative particle in which sulfur is initially uniformly distributed within its pore space. The remaining pore space not occupied by sulfur is saturated with electrolyte. In contrast to the particle model presented in earlier work,[31] all dissolved species within the particles are allowed to leave the internal pore space and enter the cell scale. In the same manner, all dissolved species on the cell scale can enter the particles. The resulting system of equations is similar to that reported by Thangavel et al.[32] The advantage of this extended

approach is that the polysulfide shuttle is now intrinsically taken into account.

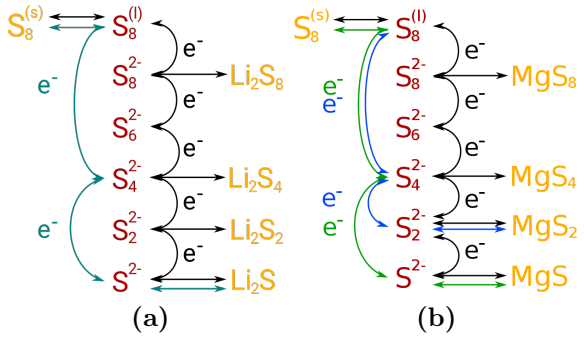

Figure 2: Sulfur redox mechanisms in Li-S (left) and Mg-S batteries (right). The reduced mechanisms, indicated by blue and green arrows, are applied in our simulations at both the cathode and anode.

3.2 Reaction mechanisms

There are several studies suggesting the reaction mechanisms for Li-S [37–40] and Mg-S [3,19–21,41,42] batteries. Generally, similar reduction and oxidation mechanisms are assumed in both systems. However, the final discharge product of Mg-S batteries using the HMDS electrolyte is a matter of discussion. Most studies, as well as our own experiments, show discharge capacities that reach only half of the theoretical limit. One explanation for this result might be the very slow kinetics for the last reduction step from MgS_2 to MgS. In this case, MgS forms only to a minor extent under normal cell operation. Certainly, the identification of the reaction intermediates is a critical task in the development of Me-S batteries, and additional effects reduce the battery capacity, such as the polysulfide shuttle or the degradation of the structural integrity of composite cathodes during cycling.

The existence of solid discharge products within the Mg-S reaction pathway could not be conclusively proven in the literature. While there are reports of solid MgS product using X-ray absorption near edge spectroscopy (XANES) and resonant inelastic X-ray scattering (RIXS), the existence of solid discharge products within the Mg-S reaction pathway could not be found by XRD. [19] These uncertainties are possibly due to the amorphous nature of the solid reduction products. [43] Furthermore, the results of different reports are not transferable

because most studies use different electrolyte and solvent systems.

Because the identification of intermediates is still lacking, especially for the Mg-S system, we use a reduced number of representative intermediate species in our simulations. In our previous work,[29,31] we demonstrated that a reduced reaction mechanism at the cathode is still able to reproduce the main features of the discharge curve of Li-S batteries.[29] To investigate the kinetics of the sluggish last conversion step from MgS_2 to MgS, we use two different reduced reaction mechanisms for Mg-S cells that end with MgS_2 and MgS. The proposed reduced reaction pathways in Li-S and Mg-S batteries are shown in Fig. 2.

For both systems, $S_8^{(s)}$ first dissolves in the electrolyte

$$S_8^{(s)} \rightleftharpoons S_8^{(l)}, \tag{1}$$

where $S_8^{(l)}$ is reduced to S_4^{2-}

$$1/4\ S_8^{(l)} + e^- \rightleftharpoons 1/2\ S_4^{2-}, \tag{2}$$

which then forms a metal-sulfur compound dissolved in the electrolyte. Depending on the final discharge product (cf. Fig. 2), S_4^{2-} is, in a subsequent step, reduced to S_2^{2-}

$$1/2\ S_4^{2-} + e^- \rightleftharpoons S_2^{2-}, \tag{3}$$

and S^{2-}

$$1/6\ S_4^{2-} + e^- \rightleftharpoons 4/6\ S^{2-} \tag{4}$$

respectively. Finally, the solid discharge products MgS_2, MgS and Li_2S precipitate according to

$$S_2^{2-} + Mg^{2+} \rightleftharpoons MgS_2, \tag{5}$$

$$S^{2-} + Mg^{2+} \rightleftharpoons MgS, \tag{6}$$

$$S^{2-} + 2\,Li^{+} \rightleftharpoons Li_2S. \tag{7}$$

The metal anode is typically rather thick, and a sufficient supply of Li and Mg can be assumed. The stripping and plating reaction is described by

$$1/2\,Mg^{2+} + e^{-} \rightleftharpoons 1/2\,Mg \tag{8}$$

and

$$Li^{+} + e^{-} \rightleftharpoons Li. \tag{9}$$

All the reactions given above are assumed to be reversible. Note that with the same mech-

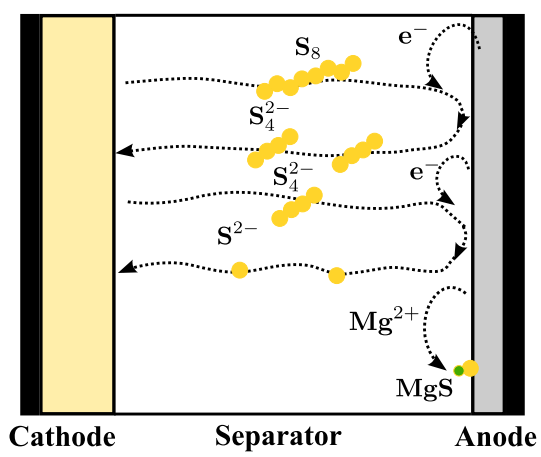

Figure 3: Schematic of the polysulfide shuttle and loss of active material due to side reactions on the anode surface assuming MgS as the final reduction product. The shuttle of different species between electrodes is represented by dotted lines.

anism, we also take into account sulfur reduction, oxidation and dissolution/precipitation

reactions at the metal anode. This step is important to describe the polysulfide shuttle.[29] In combination with the transport (shuttle) of polysulfide species at the cell scale, this approach allows for simulation of the self-discharge, decrease of the coulombic efficiency, and capacity fade of Me-S batteries.

The rate of the reactions given by Eqs. (1)-(9) is modeled by a Butler-Volmer-type expression[44,45]

$$r_m = k_f^0 \frac{a_{\text{ed.}}^{1-\alpha} a_{\text{prod.}}^{\alpha}}{\gamma_{\ddagger}} (e^{-\frac{\alpha}{RT}\Delta\bar{\mu}_m} - e^{\frac{1-\alpha}{RT}\Delta\bar{\mu}_m}), \tag{10}$$

where k_f^0 is the frequency factor, R is the ideal gas constant, T is the temperature, α is the symmetry factor, $\ddagger$ is the activity coefficient of the transition state, $\Delta\bar{\mu}_m$ is the electrochemical potential difference of reaction m, and $a_{\text{ed.}}$ and $a_{\text{prod.}}$ are the activity products of educts and products, respectively. The electrochemical potential difference of the charge-transfer reaction m can be calculated according to

$$\Delta\bar{\mu}_m = nF(\phi_{\text{elode}} - \phi_{\text{elyte}} - U_{\text{eq}}), \tag{11}$$

where n is the number of electrons transferred during the reaction and F is the Faraday constant. ϕ_{elode}, ϕ_{elyte} and U_{eq} are the potential of the electrode, the potential of the electrolyte and the equilibrium potential, respectively. The equilibrium potential can be calculated by the Nernst equation

$$U_{\text{eq}} = U_{\text{eq}}^{\ominus} + \frac{RT}{nF} \ln\left(\frac{a_{\text{ed.}}}{a_{\text{prod.}}}\right), \tag{12}$$

where $U_{\text{eq}}^{\ominus}$ is the equilibrium potential in the reference state.

The chemical potential difference for precipitation/dissolution reactions can be obtained by

$$\Delta\bar{\mu}_m = RT \ln\left(K_{\text{sp}} \frac{a_{\text{ed.}}}{a_{\text{prod.}}}\right), \tag{13}$$

where K_{sp} is the solubility product of dissolved species. The products of the activities $a_i = \frac{c_i}{c_{\text{ref}}}$ are given by

$$a_{\text{ed.}} = \prod_{\text{i=ed.}} a_i^{|\nu_{i,m}|} \text{ and } a_{\text{prod.}} = \prod_{\text{i=prod.}} a_i^{|\nu_{i,m}|}, \tag{14}$$

where $\nu_{i,m}$ are the stoichiometric coefficients of the reactions. The reference conditions are chosen arbitrarily as $c_{\text{ref}} = 1$ mol/m^3, and the activity for all solids is, by definition, equal to 1.

3.3 Governing Equations

The cell model describing the cell scale and the particle model describing the particle scale are described by 1D continuum models with Cartesian (denoted by x) and spherical (denoted by r) coordinates, respectively. The aim of this approach is to include the geometrical complexity and the most important physicochemical phenomena without incurring a computational cost. A schematic image of the simulation geometry is shown in Fig. 1.

The transport of species at the cell and particle scales is described by the Nernst-Planck equation, neglecting contributions due to the convection of the electrolyte. The resulting set of equations is often referred to as dilute solution theory because interactions between the dissolved species in the electrolyte are neglected.

At the cell scale, the transport of species i_{cell} is given by

$$\vec{N}_{i_{\text{cell}}} = -D^{\text{eff}}_{i_{\text{cell}}} \frac{\partial c_{i_{\text{cell}}}}{\partial x} - D^{\text{eff}}_{i_{\text{cell}}} c_{i_{\text{cell}}} \frac{z_i F}{RT} \frac{\partial \phi_{\text{elyte}_{\text{cell}}}}{\partial x}. \tag{15}$$

The Nernst-Planck equation in spherical coordinates describing the flux of species i_{part} at the particle scale follows as

$$\vec{N}_{i_{\text{part}}} = -D^{\text{eff}}_{i_{\text{part}}} \frac{\partial c_{i_{\text{part}}}}{\partial r} - D^{\text{eff}}_{i_{\text{part}}} c_{i_{\text{part}}} \frac{z_i F}{RT} \frac{\partial \phi_{\text{elyte}_{\text{part}}}}{\partial r}. \tag{16}$$

The first term describes the diffusive transport of species i_{d} in domain d (d = cell, particle) due to a gradient in concentration $c_{i_{\text{d}}}$. $D^{\text{eff}}_{i,\text{d}}$ is the effective diffusion coefficient given by the Bruggeman correlation

$$D^{\text{eff}}_{i_{\text{d}}} = D^{0}_{i_{\text{d}}} \varepsilon^{\beta_{\text{d}}}_{\text{elyte}_{\text{d}}}, \tag{17}$$

where $D^{0}_{i_{\text{d}}}$ is the bulk diffusion coefficient and β_{d} is the Bruggeman coefficient, which is, in this work, chosen to be 1.5 and 10 for the cell and particle scales, respectively. At the particle scale, the Bruggeman coefficient is considerably larger to describe the complex nanometer-sized pores of the particles. The conservation of mass of species i in the electrolyte needs to be solved at the particle scale and cell scale. Note that, in this approach, the additional particle scale is only solved in the cathode domain.

At the *cell scale*, the conservation of mass is given by

$$\frac{\partial \varepsilon_{\text{elyte}_{\text{cell}}} c_{i_{\text{cell}}}}{\partial t} = -\frac{\partial \vec{N}_{i_{\text{cell}}}}{\partial x} + S_{i_{\text{cell}}}, \tag{18}$$

where $\vec{N}_{i_{\text{cell}}}$ is the flux of species icell introduced above and $S_{i_{\text{cell}}}$ represents a source term. Within the cathode domain, the source term is given by

$$S_{i_{\text{cell}}} = a^{V}_{\text{SC}_{\text{cell}}} (\psi_{\text{open}} \sum_{m} \nu_{i,m} r_m + (1 - \psi_{\text{open}}) \vec{N}_{i_{\text{ex}}}), \tag{19}$$

where the term $a^{V}_{\text{SC}_{\text{cell}}} N_{i_{\text{ex}}}$ describes the exchange of mass between the particle scale and cell scale on the particle surface. ψ_{open} is an additional factor describing the open porosity of

the particles, and we assume a value of 0.5 in our simulations. Assuming spherical particles, the surface $a^V_{\mathrm{SC_{cell}}}$ cell is given by the particle size R_p and the volume fraction $\varepsilon_{\mathrm{SC_{cell}}}$ of the sulfur-carbon composite

$$a^V_{\mathrm{SC_{cell,0}}} = \frac{3\varepsilon_{\mathrm{SC_{cell}}}}{R_p}. \tag{20}$$

The reactions on the anode surface are treated as boundary conditions and are presented in the following paragraph.

At the *particle scale*, species conservation is given by

$$\frac{\partial \varepsilon_{\mathrm{elyte_{part}}} c_{i_{\mathrm{part}}}}{\partial t} = -\frac{1}{r^2}\frac{\partial r^2 \vec{N}_{i_{\mathrm{part}}}}{\partial r} + \sum_m a^V_{\mathrm{part}} \nu_{i,m} r_m, \tag{21}$$

In our model, we use the charge conservation equation in the electrolyte to determine the local electrolyte potential at the cell scale and particle scale:

$$0 = \sum_i z_i F \left(\sum_m a^V_{\mathrm{d}} \nu_{i,m} r_m - \nabla \vec{N}_{i_{\mathrm{d}}} \right), \tag{22}$$

where z_i is the charge number of the corresponding species i and $\vec{N}_{i_{\mathrm{d}}}$ is the corresponding flux in domain d. The active surface area differs between electrochemical and chemical reactions. Following the approach of Kumaresan et al.,[24] the active surface area of the electrochemical reactions within the cathode is described by

$$a^V_{\mathrm{SC_d}} = a^V_{\mathrm{SC_{d,0}}} \left(\frac{\varepsilon_{\mathrm{elyte_d}}}{\varepsilon_{\mathrm{elyte_{d,0}}}} \right)^{\xi}, \tag{23}$$

Where ξ is an empirical parameter describing the morphology of the active surface. We set this parameter to 1.5 in our simulations. $a^V_{\mathrm{SC_{d,0}}}$ and $\varepsilon_{\mathrm{elyte_{d,0}}}$ are the initial active surface area and the initial volume fraction of the electrolyte, respectively. This is a relatively practical but crude approach, and more involved solutions are presented in the literature.[46,47] The

volume fraction of the electrolyte $\varepsilon_{\mathrm{elyte_d}}$ is given by

$$\varepsilon_{\mathrm{elyte_d}} = 1 - \varepsilon_{\mathrm{SC_d}} - \sum_k \varepsilon_{k_\mathrm{d}}. \tag{24}$$

The change of the volume fraction $\varepsilon_{k_\mathrm{d}}$ of precipitate k due to formation and dissolution is described by

$$\frac{\partial \varepsilon_{k_\mathrm{d}}}{\partial t} = -\frac{MW_k}{\rho_k} \sum_m a^V_{k_\mathrm{d}} \nu_{i,m} r_m, \tag{25}$$

where MW_k is the molecular weight and ρ_k is the density of precipitate k. The reaction source term depends on the specific surface area of precipitate $a^V_{k_\mathrm{d}}$. Following the approach presented in Ref. 24, the relation between the surface area and volume fraction of the precipitate is considered by an empirical correlation

$$a^V_{k_\mathrm{d}} = a^V_{\mathrm{SC_{d,0}}} \varepsilon_\mathrm{k}. \tag{26}$$

This approach provides a crude approximation of the precipitation process,[31] which mostly leads to an overprediction of the corresponding effects. Still, this phenomenological approach allows for qualitative simulation of nucleation effects without implementing a more involved theory for the nucleation and growth of solid charge and discharge products.[46–48]

The charge transport in the solid phase at the electrode scale is described by Ohm's law

$$0 = -\kappa^{\mathrm{eff}}_{\mathrm{elode}} \frac{\partial \phi_{\mathrm{elode_{cell}}}}{\partial x} - a^V_{\mathrm{SC_{cell}}} i_F^{\mathrm{part}} - i_F^{\mathrm{cell}}, \tag{27}$$

where $\kappa^{\mathrm{eff}}_{\mathrm{elode_{cell}}}$ is the effective conductivity of the electrode given by the Bruggemann correlation

$$\kappa^{\mathrm{eff}}_{\mathrm{elode}} = \kappa_{\mathrm{SC}} \varepsilon^{1.5}_{\mathrm{SC_{cell}}}. \tag{28}$$

In comparison to the liquid electrolyte, the conductivity of carbon particles is rather high. Furthermore, the particle size is rather small, such that the potential within one representative carbon particle is assumed to be constant. The specific Faradaic current i_F^{part} originating from the electrochemical reactions within the particle can be obtained by integrating over the local reaction rates

$$i_F^{\text{part}} = \frac{\int_{r=0}^{r=R_{\text{p}}} 4\pi r^2 i_F(r)}{4\pi R_{\text{p}}^2}. \tag{29}$$

$i_F(r)$ is the local volumetric Faradaic current density given by the sum over all the electrochemical reactions

$$i_F(r) = \sum_m -nFa^V_{SC_{\text{part}}} r_m. \tag{30}$$

The local volumetric Faradaic current density for the macroscopic cell model is similarly given by

$$i_F^{\text{cell}} = \sum_m -nFa^V_{SC_{\text{cell}}} r_m. \tag{31}$$

3.4 Boundary conditions

In this section, we provide the corresponding boundary conditions at the cell and particle scales.

3.4.1 Cell scale

The current collector at the cathode forms a physical barrier. At this boundary, the flux of each species is set to zero

$$\vec{N}_{i_{\text{cell}}}\Big|_{x=0} = 0. \tag{32}$$

Furthermore, all the current at this boundary flows within the solid phase and is equal to the externally applied current I. Consequently, the current density within the electrolyte is zero

$$\left.\frac{\partial \phi_{\mathrm{elyte}_{\mathrm{cell}}}}{\partial x}\right|_{x=0} = 0 \quad \text{and} \quad -\kappa^{\mathrm{eff}}_{\mathrm{elode}_{\mathrm{cell}}} \left.\frac{\partial \phi_{\mathrm{elode}_{\mathrm{cell}}}}{\partial x}\right|_{x=0} = I. \tag{33}$$

At the interface between the cathode and separator, all the current flows in the electrolyte such that the current within the solid phase is zero

$$\left.\frac{\partial \phi_{\mathrm{elode}}}{\partial x}\right|_{x=L_{\mathrm{cat}}} = 0. \tag{34}$$

The potential of the metal electrode is set as the reference

$$\left.\phi_{\mathrm{elode}_{\mathrm{cell}}}\right|_{x=L_{\mathrm{tot}}} = 0. \tag{35}$$

and the fluxes of dissolved species in the electrolyte $\left.\vec{N}_{i_{\mathrm{cell}}}\right|_{x=L_{\mathrm{tot}}}$ are given by the chemical and electrochemical reactions on the electrode surface

$$\left.\vec{N}_{i_{\mathrm{cell}}}\right|_{x=L_{\mathrm{tot}}} = \sum_m \nu_{i,m} r_m. \tag{36}$$

The corresponding current in the electrolyte is given by

$$\left.i_{\mathrm{elyte}_{\mathrm{cell}}}\right|_{x=L_{\mathrm{tot}}} = \sum_i z_i F \sum_m \nu_{i,m} r_m. \tag{37}$$

3.4.2 Particle scale

At the center of the particle $r = 0$, the flux of each species is zero due to the symmetry of the spherical model particles

$$\vec{N}_{i_{\text{part}}}\Big|_{r=0} = 0. \tag{38}$$

On the particle surface $r = R_{\text{p}}$, we allow for an exchange of species between the particle and cell scales. This flux (cf. Eq. (19)) is given by

$$\vec{N}_{i_{\text{ex}}} = -D^{\text{eff}}_{i_{\text{ex}}} \left(\frac{\partial c_{i_{\text{ex}}}}{\partial r}\Big|_{r=R_{\text{p}}} + c_{i_{\text{ex}}} \frac{z_{i_{\text{ex}}} F}{RT} \frac{\partial \phi_{\text{elyte}_{\text{part}}}}{\partial r}\Big|_{r=R_{\text{p}}} \right). \tag{39}$$

3.5 Parameters

Simulations on the continuum scale require several parameters defining the geometry, electrochemistry, transport properties, and thermodynamics of the cells at hand. In the following paragraphs, we provide the set of parameters used in the simulations presented in this article.

Structural parameters Structural parameters are obtained from our in-house experiments and are summarized in Table 1. Concentrations, volume fractions and surface areas are initial values and change during the simulations.

Transport parameters In this work, we use an electrolyte system based on a solvent mixture of TEGDME:DEGDME to enable cycling of the Mg-S battery. This system is not yet popular, and consequently, transport parameters are not reported in the literature. However, the conductivities for each of the solvents are available,[49–51] and averaging the conductivities of both solvents provides a reasonable approximation.[52] The conductivity of the Mg-S electrolyte is taken from Ref. 52 and is averaged in the same manner. The transport parameters of sulfur species are taken from Kumaresan et al.[24] All the transport parameters in this work are summarized in Table 2.

Table 1: Structural parameters from our in-house experiments. The given values for concentrations, volume fractions and surface areas are initial values and change during the simulations.

	Cell scale	Particle scale
Cathode		
Thickness/Radius	40 µm	340 nm
Volume elements	5	3
Surface area	-	$2.26 \cdot 10^8 \mathrm{m}^{-1}$
Bruggemann coefficient	1.5	10
Phases		
Carbon	0.163	0.2
Binder	0.023	-
$S_8^{(s)}$	$1 \cdot 10^{-4}$	0.209
Li_2S/MgS	$1 \cdot 10^{-4}$	$1 \cdot 10^{-4}$
Electrolyte	0.814	0.591
$((Li^+/Mg^{2+})/(A^-/A^{2-}), S_8^{(l)}, S_4^{2-}, S_2^{2-})$	(1000/1400, 19, 0.02, $1 \cdot 10^{-9}$ mol/m^3)	
Separator		
Thickness	260 µm	-
Volume elements	3	-
Thickness of volume element at anode	5 µm	-
Bruggemann coefficient	1.5	-
Phases		
Glass fiber	0.2	-
Li_2S/MgS	$1 \cdot 10^{-4}$	-
$((Li^+/Mg^{2+})/(A^-/A^{2-}), S_8^{(l)}, S_4^{2-}, S_2^{2-})$	(1000/1400, 19, 0.02, $1 \cdot 10^{-9}$ mol/m^3)	

Kinetic parameters The kinetic and thermodynamic parameters are calibrated to reproduce our experimental data. An overview of the kinetic and thermodynamic parameters can be found in Table 2.

Most of the calibration is straightforward. However, as shown in section 4.3.3, a variety of frequency parameters for anode side reactions are appropriate to reproduce the open-circuit voltage (OCV) in our experiments. However, by additionally considering the subsequent discharge, it is possible to reduce the parameter space.

We briefly illustrate this approach in the following paragraph. After the transition from the first to the second plateau, all $S_8^{(l)}$ is consumed, and the self-discharge is determined by the reduction of S_4^{2-} to S^{2-}. This discharge corresponds directly to the accessible discharge capacity measured in the subsequent discharge. By altering both frequency factors of the $S_8^{(l)}$ and S_4^{2-} reductions to simultaneously reproduce the voltage curve and discharge capacity, we obtain the set of frequency factors shown in Table 2.

Table 2: Transport, kinetic and thermodynamic parameters of species and phases in this work.

Parameter	Value	Description	Source
		Transport parameters	
Electrolyte			
$D_{\mathrm{Li^+}}/D_{\mathrm{A^-}}$	$9.3153 \cdot 10^{-11}\ \frac{\mathrm{m^2}}{\mathrm{s}}$	$\mathrm{Li^+/A^-}$ diffusion coefficient	49–51
$D_{\mathrm{Mg^{2+}}}/D_{\mathrm{A^{2-}}}$	$2.8516 \cdot 10^{-12}\ \frac{\mathrm{m^2}}{\mathrm{s}}$	$\mathrm{Mg^{2+}/A^{2-}}$ diffusion coefficient	15
$D_{\mathrm{S_8}}$	$10 \cdot 10^{-10}\ \frac{\mathrm{m^2}}{\mathrm{s}}$	$\mathrm{S_8}$ diffusion coefficient	24
$D_{\mathrm{S_4^{2-}}}$	$1 \cdot 10^{-10}\ \frac{\mathrm{m^2}}{\mathrm{s}}$	$\mathrm{S_4^{2-}}$ diffusion coefficient	24
$D_{\mathrm{S^{2-}}}$	$1 \cdot 10^{-10}\ \frac{\mathrm{m^2}}{\mathrm{s}}$	$\mathrm{S^{2-}}$ diffusion coefficient	24
Carbon			
κ_{elode}	$10\ \frac{\mathrm{S}}{\mathrm{m}}$	Electronic conductivity	*
		Kinetic parameters	
Cathode (Cell/Particle)			
$\mathbf{S_8^{(s)} \rightleftharpoons S_8^{(l)}}$			
k_f^0	$1 \cdot 10^{-1}\ /\ 1\ \frac{\mathrm{mol}}{\mathrm{m^2 s}}$	frequency factor of reaction (Li-S/Mg-S)	* / 24
K_sp	19	solubility product (Li-S/Mg-S)	25
$1/4\ \mathbf{S_8^{(l)} + e^- \rightleftharpoons 1/2\ S_4^{2-}}$			
k_f^0	$1.972 \cdot 10^{0}\ \frac{\mathrm{mol}}{\mathrm{m^2 s}}$	frequency factor of reaction (Li-S/Mg-S)	24
$U_\mathrm{eq}^\ominus$	2.45/1.65 V	OCP at reference conditions (Li-S/Mg-S)	3,24
$1/6\ \mathbf{S_4^{2-} + e^- \rightleftharpoons 4/6\ S^{2-}}$			
k_f^0	$1.971 \cdot 10^{-2}\ \frac{\mathrm{mol}}{\mathrm{m^2 s}}$	frequency factor of reaction (Li-S/Mg-S)	24
$U_\mathrm{eq}^\ominus$	2.0/1.1 V	OCP at reference conditions (Li-S/Mg-S)	3,24
$\mathbf{S^{2-} + Mg^{2+} \rightleftharpoons MgS}$			
k_f^0	$1 \cdot 10^{-1}\ \frac{\mathrm{mol}}{\mathrm{m^2 s}}$	frequency factor of reaction	*
K_sp	$1 \cdot 10^{5}$	solubility product	*
$\mathbf{S^{2-} + 2\ Li^+ \rightleftharpoons Li_2S}$			
k_f^0	$1 \cdot 10^{-1}\ \frac{\mathrm{mol}}{\mathrm{m^2 s}}$	frequency factor of reaction	*
K_sp	$1 \cdot 10^{5}$	solubility product	*
Anode			
$\mathbf{Li^+ + e^- \rightleftharpoons Li^{(s)}}$			
k_f^0	$4 \cdot 10^{-1}\ \frac{\mathrm{mol}}{\mathrm{m^2 s}}$	frequency factor of reaction	*
$\mathrm{U_{eq}^\ominus}$	0 V	Li reference electrode	*
$\mathbf{1/2\ Mg^{2+} + e^- \rightleftharpoons 1/2\ Mg^{(s)}}$			
k_f^0	$4 \cdot 10^{-1}\ \frac{\mathrm{mol}}{\mathrm{m^2 s}}$	frequency factor of reaction	*
$\mathrm{U_{eq}^\ominus}$	0 V	Mg reference electrode	*
$\mathbf{1/4\ S_8^{(l)} + e^- \rightleftharpoons 1/2\ S_4^{2-}}$			
k_f^0	$3 \cdot 10^{-22}\ /\ 6 \cdot 10^{-16}\ \frac{\mathrm{mol}}{\mathrm{m^2 s}}$	frequency factor of reaction (Li-S/Mg-S)	*
$\mathrm{U_{eq}^\ominus}$	2.45/1.65 V	OCP at reference conditions (Li-S/Mg-S)	*
$\mathbf{1/6\ S_4^{2-} + e^- \rightleftharpoons 4/6\ S^{2-}}$			
k_f^0	$2.3 \cdot 10^{-19}\ /\ 6 \cdot 10^{-10}\ \frac{\mathrm{mol}}{\mathrm{m^2 s}}$	frequency factor of reaction (Li-S/Mg-S)	*
$\mathrm{U_{eq}^\ominus}$	2.0/1.1 V	OCP at reference conditions (Li-S/Mg-S)	*
$\mathbf{S^{2-} + 2\ Li^+ \rightleftharpoons Li_2S}$			
k_f^0	$1 \cdot 10^{-1}\ \frac{\mathrm{mol}}{\mathrm{m^2 s}}$	frequency factor of reaction	*
K_sp	$1 \cdot 10^{5}$	solubility product	*
$\mathbf{S^{2-} + Mg^{2+} \rightleftharpoons MgS}$			
k_f^0	$1 \cdot 10^{-1}\ \frac{\mathrm{mol}}{\mathrm{m^2 s}}$	frequency factor of reaction	*
K_sp	$1 \cdot 10^{5}$	solubility product	*
		Thermodynamic parameters	
$\mathbf{S_8^{(s)}}$			
$\rho_{\mathrm{S_8}}^{(s)}$	$2070.4\ \frac{\mathrm{kg}}{\mathrm{m^3}}$	Density	53
$\mathrm{MW_{S_8}^{(s)}}$	$0.2565\ \frac{\mathrm{kg}}{\mathrm{mol}}$	Molecular weight	53
$\mathbf{Li_2S}$			
$\rho_{\mathbf{Li_2S}}$	$1659\ \frac{\mathrm{kg}}{\mathrm{m^3}}$	Density	54
$\mathrm{MW}_{\mathbf{Li_2S}}$	$0.0459\ \frac{\mathrm{kg}}{\mathrm{mol}}$	Molecular weight	54
MgS			
$\rho_{\mathbf{MgS}}$	$2680\ \frac{\mathrm{kg}}{\mathrm{m^3}}$	Density	54
$\mathrm{MW}_{\mathbf{MgS}}$	$0.0563\ \frac{\mathrm{kg}}{\mathrm{mol}}$	Molecular weight	54

* fit to experimental data

4 Results

In this section, we present the results of our measurements and simulations of Me-S batteries. First, we provide a short discussion of our measurements before comparing them to simulations to validate our model. Based on these results, we present a comprehensive parameter study to determine the most important material properties affecting the self-discharge of Me-S batteries.

4.1 OCV measurements

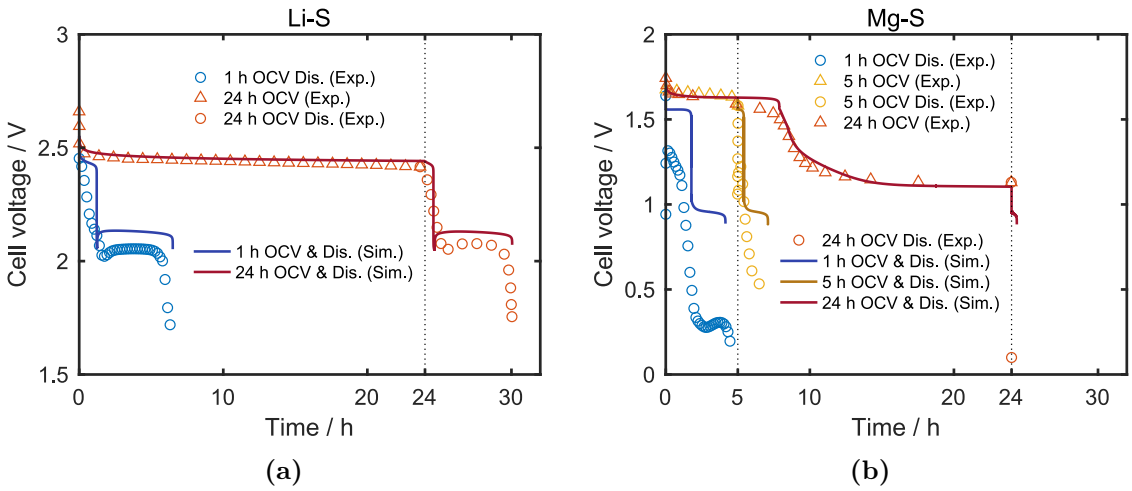

Figure 4: Cell voltage of Li-S (left) and Mg-S (right) cells during storage under open-circuit conditions for 1, 5, and 24 h. Subsequently, the cells are discharged at a rate of C/10. The symbols and solid lines represent experimental and simulated data, respectively.

Fig. 4 compares the cell voltage predicted by our simulations (solid lines) with the corresponding experimental data (open symbols). The blue symbols represent the measured cell voltage during 1 h of rest under open-circuit conditions and the subsequent C/10 discharge process. The red symbols in Fig. 4 represent the measured cell voltage of Li-S and Mg-S cells during a 24-h rest period and a subsequent C/10 discharge. For the Mg-S system, an additional measurement with a rest period of 5 h is performed to resolve the dynamics of the self-discharge and the corresponding capacity loss of the first discharge. In our experiments, we find, for both the Li-S and Mg-S systems, a measurable self-discharge during 24 h of

storage under open-circuit conditions.

After a steep initial drop, the cell voltage of the Li-S cell stabilizes at approximately 2.45 V, and a minor drift in the voltage signal can be observed during the 24 h measurement time. In the subsequent discharge, the upper voltage plateau associated with the reduction of S_8 to S_4^{2-} only makes a minor contribution to the overall cell capacity, which indicates that most of the dissolved sulfur is already reduced at the anode and is responsible for most of the capacity loss. In the Li-S literature,[4,27,55] this effect is mainly associated with the polysulfide shuttle. Our measurements suggest similar processes in Mg-S batteries.

Mg-S cells exhibit a similar initial drop in cell voltage with a subsequent plateau at approximately 1.6 V. However, in contrast to Li-S cells, the voltage does not stabilize, and we observe a second drop in cell voltage after approximately 10 h. The final cell voltage is approximately 1.15 V. The shape of the OCV is comparable to the cell voltage during slow discharge of the battery, which indicates that the self-discharge during storage is much more pronounced in Mg-S cells than in Li-S cells. Interestingly, Mg-S cells show, after 1 h of storage, a higher capacity at the first plateau than the Li-S system. However, we could not observe a self-limiting process as in Li-S batteries resulting in complete self-discharge within 24 hours.

Additionally, the drop in cell voltage after applying a current is more pronounced than in the Li-S system. In this context, it should be noted that it cannot be excluded that a decomposition of the electrolyte salt leads to a reduction of sulfur at the cathode. A similar polysulfide shuttle behavior was reported in Ref. 14, but it was not investigated in more detail. Additional figures comparing the self-discharge of Li-S and Mg-S batteries, as well as additional results of the Mg-S storage experiments, can be found in Fig. S1 and Fig. S2.

To illustrate the self-discharge dynamics, we try to quantify the capacity loss during storage after different rest periods. Table 3 shows the discharge capacities of the two cells after the different rest periods. In Li-S batteries, the self-discharge is approximately 650 mAh/g_S within 24 h. However, most of this loss (600 mAh/g_S) is already observed within the first

hour after cell assembly. This finding indicates either that the initial degradation processes are extremely fast or that the cathode performance suffers from relatively poor sulfur utilization. Our simulations support the latter, and additional simulation results with high sulfur utilization are included as supporting information in Fig. S3. A detailed discussion can be found in the sections below.

In the case of the Mg-S system, the self-discharge is much more pronounced. After a 24-h rest period, practically no capacity can be measured, and we perform an additional experiment with a 5-h rest period to quantify the self-discharge rate. However, it cannot be excluded that, also after 24 h, there are still sulfur species in the battery, which can be reduced; however, high overpotentials at the beginning of the discharge might cause a drop of the cell voltage below the cut-off voltage.

Based on the capacity loss, we calculate the self-discharge rate I_{self}. For Mg-S batteries, I_{self} is approximately 200 mAh/g_S, which would be even larger than the current density of the subsequent C/10 discharge. This is an interesting observation because it indicates that charging the battery at low currents is, in practice, exceedingly difficult. Furthermore, we use this self-discharge rate to estimate the total capacity of the electrodes

$$C_{\text{comb.}} = t_{\text{OCV}} I_{\text{self}} + t_{\text{CC}} I_{\text{self}} + t_{\text{CC}} I_{\text{C/10}}, \tag{40}$$

where t_{OCV} is the time under open-circuit conditions, t_{CC} is the discharge time with constant current, and $I_{\text{C/10}}$ is the discharge current.

In our measurements, the combined capacity of Mg-S cells is slightly higher than the theoretical capacity. The corresponding capacities of all cells are shown in Table 3, which indicates that the self-discharge is faster in the initial stage of the OCV measurements. Similar results have been reported for Li-S cells. Here, it was shown that the self-discharge of Li-S cells depends on the state of charge and is slower than that of Mg-S cells under dynamic

conditions.[55]

Furthermore, it cannot be excluded that capacity losses due to side reactions contribute to the capacity in the first cycle. The identification of these side reactions and their implications for cell performance is certainly another crucial aspect in the development of Mg-S batteries. Our simulations provide an additional tool for interpreting the experimental data, and in the following paragraphs, we demonstrate how the different material properties affect the self-discharge of Me-S cells.

Table 3: Discharge capacities and combined capacities of self-discharge and discharge after different rest periods. The duration of discharge is given in brackets.

Rest period	**Discharge capacity mAh/g_S**		**Combined capacity mAh/g_S (Discharge duration)**	
h	Li-S	Mg-S	Li-S	Mg-S
1	1063	768	1078 (6.35 h)	1886 (4.59 h)
5	-	309	-	1859 (1.75 h)
24	1008	0	1063 (6.09 h)	-

4.2 Model validation

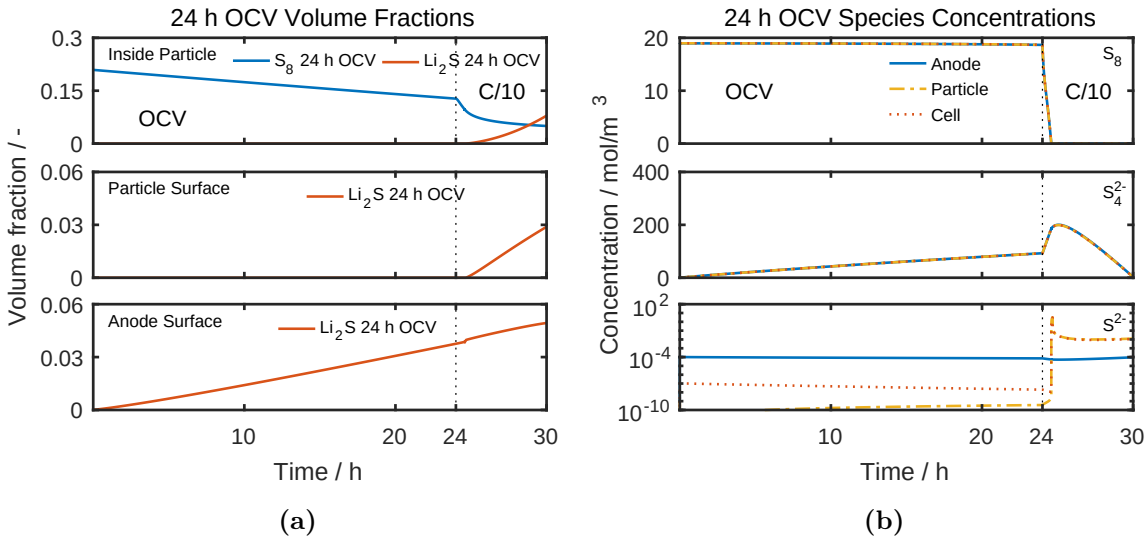

Figure 5: Analysis of the 24-h OCV measurement and subsequent discharge of a Li-S cell. a) Average volume fractions of S_8 and Li_2S within the micropores, on the particle surface and on the anode surface. b) Average concentrations of polysulfides at the cathode on particle and cell scale and at the anode.

In the literature, there are a variety of parameter sets describing the discharge behavior of Li-S batteries, which can serve as a starting point for model parameterization. However, because this is the first attempt to derive a continuum model for Mg-S batteries, there is practically no suitable source of model parameters in the literature. Moreover, the characterization of processes and materials in the Mg-S system is still lacking. Only a few parameters can be taken from the literature, such as the conductivity of the Mg-S electrolyte. Other parameters need to be calibrated against the experimental data. The right column of Table 2 gives an overview of the parameters, which are fitted to experimental data under various conditions.

As discussed above and shown in Fig. 3, the self-discharge in our model is described by also allowing sulfur redox reactions and discharge product precipitation at the anode. Thereby, polysulfides that diffuse from the cathode to the anode can be reduced at the anode surface. Finally, they can form either a Li_2S or MgS precipitate on the anode surface. Intermediate polysulfide species that do not precipitate can diffuse back to the cathode and change the species concentrations there. This change in concentration influences the cathode potential as described by Eq. 12 and can be observed in the cell voltage.

4.2.1 Li-S cell

In the first part of this section, we focus on describing the simulation results of Li-S cells with the parameters given in Table 1. These parameters are able to reproduce the experimental data. In Fig. 4, the simulated OCV measurements and the subsequent discharge curves are shown by solid lines. The corresponding experimental data are given by open symbols. The left panel shows the simulated behavior of the Li-S system, which is in good agreement with the experiments. Our simulations reproduce the voltage trend during OCV. Additionally, the capacity fade of approximately 50 mAh/g_S due to the self-discharge after 24 h is also in qualitative agreement. The corresponding evolutions of the concentrations in the electrolyte and solid-phase volume fractions are summarized in Fig. 5.

Open-circuit conditions Fig. 5 a) presents the average volume fractions of S_8 and Li_2S. In our simulations, we do not observe any spatial gradients. The top, middle and bottom panels correspond to the volume fractions inside the particles, the volume fraction of Li_2S on the particle surfaces, and the volume fraction of Li_2S on the anode surface, respectively. The simulations of the Li-S cell predict that a significant amount of solid sulfur continuously dissolves in the electrolyte during the 24-h rest period. Even after 24 h, a considerable amount of sulfur remains inside the particles and continuously provides $S_8^{(l)}$. The average concentrations within the cathode are shown in Fig. 5 b). Consistent with the simulated volume fractions, we do not observe any spatial gradients. In particular, the concentration gradient between the particle scale and the cell scale is only minor. The S_8 concentration is always close to the solubility limit of 19 mol/m^3 concentration slightly increases at a constant rate, but a significant reduction to S^{2-} is not observed, which also explains why no transition between the first and second plateau is visible in the OCV measurements of Li-S cells.

C/10 discharge The reduction of S_4^{2-} immediately increases when the subsequent discharge begins, resulting in a significant precipitation of Li_2S within the particles and on the cathode particle surface. To reduce the shuttle effect, a precipitation of discharge products within the particles is preferable. Indeed, most of the discharge product is observed inside the particle pores, and only a minor fraction precipitates on the particle surface. This is due to the constant supply of dissolved sulfur from the solid $S_8^{(s)}$ in the particle pores, which is only partially utilized. This poor utilization is considered in our simulations by the lower frequency factor of the $\mathbf{S}_8^{(s)} \rightleftharpoons \mathbf{S}_8^{(l)}$ reaction. However, due to the homogeneous distribution of dissolved polysulfides, precipitation of discharge products on the particle surface is unavoidable. A similar mechanism leads to the precipitation of Li_2S on the anode surface. As discussed above, sulfur redox reactions at the anode produce only a small amount of S^{2-} such that the precipitation of Li_2S on the anode during discharge depends on the diffusion of S^{2-} from cathode to anode. Most of S^{2-} is consumed within the micropores, and the amount

that leaves the micropores is mostly consumed within the macropores of the cathode. The positions of the discharge plateaus differ from the experimental results. In our simulations, we use the frequency factors for the sulfur reduction at the cathode given by Kumaresan et al.[24] For a better fit, the frequency factors need to be adapted to the system at hand, but in this article, we want to focus only on the self-discharge. In this case, the reduction kinetics at the cathode have a negligible effect, as shown in Fig. S5. Under open-circuit conditions, the cathode only acts as a kind of reference electrode.

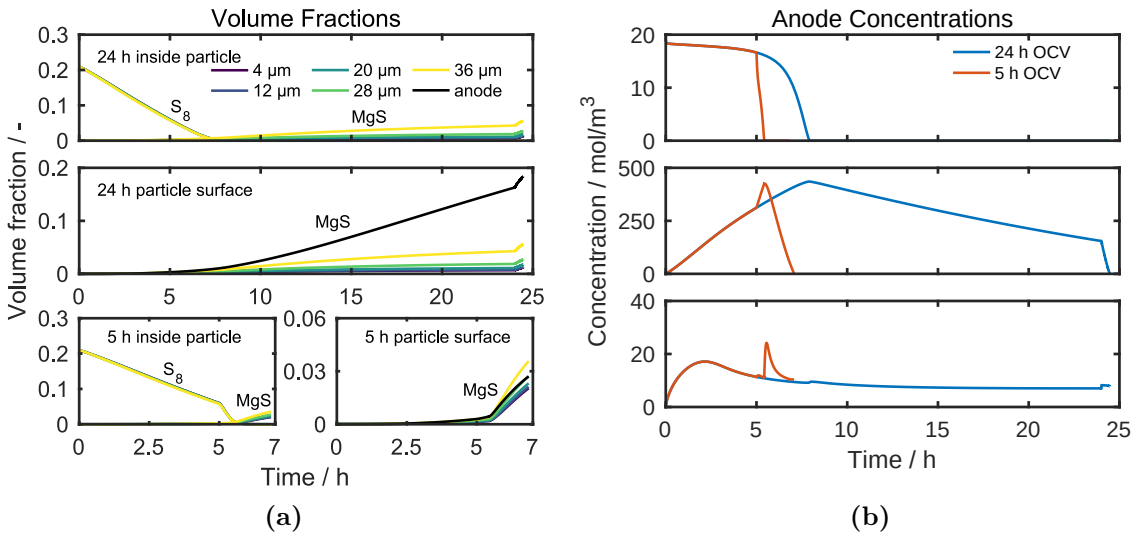

Figure 6: Analysis of the OCV measurements and subsequent discharge of an Mg-S Cell. a) Volume fractions of S_8 and MgS within the particle and on cell scale. Different colors represent volume fractions at varying distances from the cathode current collector. b) Concentrations of polysulfides at the anode.

4.2.2 Mg-S cell

The solid lines in the right panel of Fig. 4 show the simulated cell voltage over time, and the open symbols represent the experimental data discussed in Section 4.1. The simulations of the Mg-S cells favorably reproduce the OCV measurements. The evolutions of solid and dissolved species within the cell provide insights for a better interpretation of the cell voltage.

Open-circuit conditions Fig. 6 presents the evolutions of solid and dissolved species during measurements under open-circuit conditions at different positions in the cell. Fig.

6 a) shows the volume fractions of S_8 and MgS for different parts of the cell and different rest periods. For the 24-h-rest-period case, the solid sulfur within the particles quickly and completely enters the solution. Compared to Li-S batteries, these fast processes lead to a small, yet visible gradient in the S_8 volume fraction within the cathode. Finally, we observe smaller volume fractions near the separator and higher volume fractions near the current collector. The corresponding concentrations of dissolved polysulfides at the anode are shown in Fig. 6 b). At the anode, S_8 is entirely reduced to S_4^{2-}, leading to a transition from the upper to lower plateau. Within the lower plateau, S_4^{2-} is then reduced to S^{2-}. A precipitation of the solid discharge product MgS at the anode can be observed. A precipitation within the particles and on the particle surface also takes place and builds up a significant gradient along the x-axis with an increasing volume fraction towards the separator.

C/10 discharge The subsequent discharge after the 24-h rest period has only a small effect on concentrations and volume fractions because the cell is almost completely discharged. Only the S^{2-} concentration shows a small peak at the beginning of discharge. The case with the 5-h rest period shows a different behavior. The evolution of concentrations and species during the rest periods under open-circuit conditions is, of course, the same as in the 24-h case, but the subsequent discharge already starts in the upper voltage plateau, which causes a sudden increase in the S_4^{2-} and S^{2-} concentrations, as observed in the Li-S simulations. Furthermore, at the beginning of discharge, only small amounts of MgS have been formed at the anode. The MgS volume fraction significantly increases during the subsequent discharge. Still, the concentration of polysulfides is higher in the cathode, which causes preferential MgS growth close to the separator, in contrast with the 24-h case, in which the subsequent discharge also leads to preferential precipitation at the anode.

As described above, similar steps occur in Li-S cells, but the processes in the Mg-S system need to be significantly faster to reproduce the experimental data. By taking such fast kinetics for side reactions into account, the simulations reproduce the trend of the discharge

capacities with increasing rest periods.

In our simulation of Mg-S cells, we consider reductions to both MgS and MgS_2. However, only the reduction to MgS fits reasonably well to the experimental data. This finding agrees with recent results published by Xu et al.,[43] which indicate that full conversion of sulfur is possible if the kinetic limitations can be reduced. Therefore, we will use the reduction mechanism to MgS in the remainder of this article.

We analyze the different processes contributing to the self-discharge of Li-S and Mg-S batteries in the next section.

4.3 Parameter study

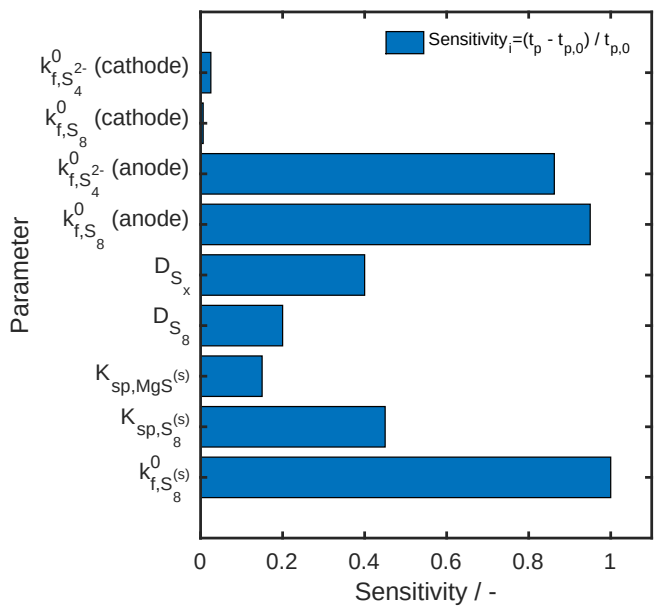

Figure 7: Sensitivity analysis of kinetic and transport parameters. Sensitivity refers to the duration of the upper plateau.

In the determination of the model parameters, we assumed that the self-discharge is kinetically limited by the side reactions of polysulfides at the anode. However, the determination of the model parameters is not unambiguous, and the self-discharge might also be strongly influenced by other properties, such as the diffusion or solubility of polysulfides. To identify the parameters that have the largest impact on the self-discharge, we perform

a sensitivity analysis of the transport and kinetic parameters. This analysis focuses on the Mg-S system, in which the self-discharge is quick and easy to quantify due to the drop in cell voltage to the second plateau. Fig. 7 presents the values of the sensitivity of key transport and kinetic parameters examined in the study. In this case, we define the sensitivity of a parameter i by the change in length of the upper plateau according to

$$\text{Sensitivity}_i = \frac{t_\text{p} - t_\text{p,0}}{t_\text{p,0}}. \tag{41}$$

Here, $t_\text{p,0}$ is the length of the upper plateau with the parameters given in Table 2, and t_p is the length with parameter i modified by one order of magnitude, which provides a quantitative measure of the influence of different parameters on self-discharge. The sensitivities shown in Fig. 7 refer to an elongation of the upper plateau. For this purpose, all parameters except the parameter $K_\text{sp,MgS}$ have been reduced by one order of magnitude. The parameter $K_\text{sp,MgS}$ was increased by one order of magnitude.

As expected, the kinetic parameters at the cathode have only a small effect on the self-discharge of Mg-S batteries. Moreover, the mobility of polysulfide species and the precipitation of MgS have a moderate effect on the self-discharge dynamics. The parameters with the highest sensitivity are the kinetic factors of the electrochemical side reactions and sulfur dissolution at the anode. This result underlines that the solubility of polysulfides is clearly key to reducing the self-discharge in Me-S batteries. A detailed discussion is given below. However, in the same solvent, we expect similar dissolution kinetics for both the Li-S and Mg-S systems. Therefore, this parameter does not explain the accelerated self-discharge of Mg-S batteries. The kinetics of the side reactions at the anode also exhibit very high sensitivity. We expect significant differences between surface properties of Mg and Li metal. Therefore, we conclude that, most likely, simple sulfur reduction kinetics on Mg are responsible for the rapid self-discharge of Mg-S batteries. In the sections below, we conduct a parameter study for each case, evaluate the results of the simulations, and show how each aspect influences

the self-discharge of the battery.

4.3.1 Solid phase kinetics and solubility

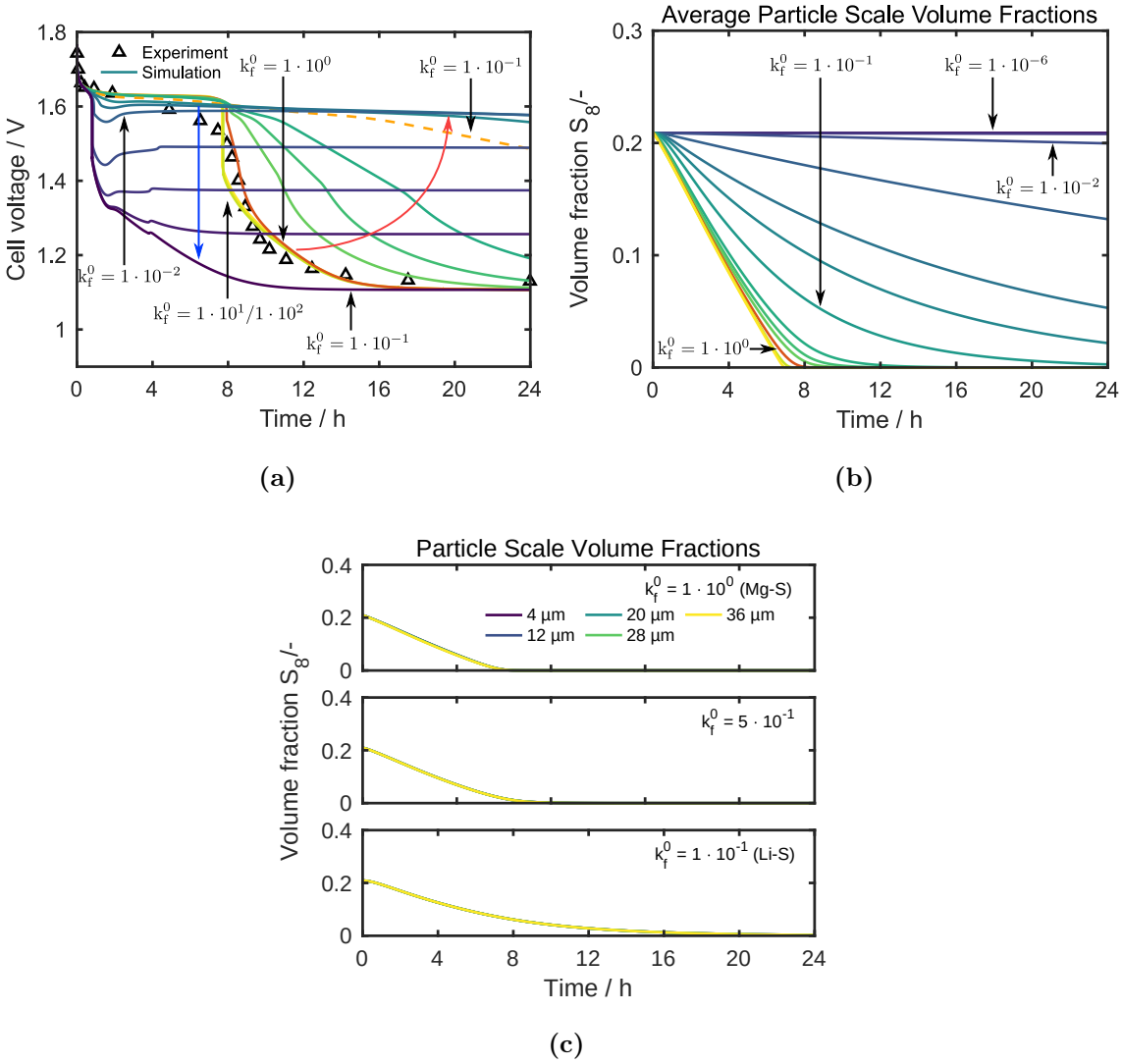

Figure 8: Variation of the dissolution kinetics. a) The OCV for different frequency factors, where the solid lines represent simulations and the symbols represent experimental data. b) Average volume fraction of solid S_8 within the microscopic pores. c) Spatial distribution of the volume fraction of solid S_8 along the x-axis from the current collector to separator. In a), the red and dashed orange curves represent the standard parameters for Mg-S and Li-S cells, respectively. The values of the frequency factors are given in mol/m^{2}s.

An important characteristic of both the Li-S and Mg-S systems is the formation of solid end products during charge and discharge. In both systems, solid sulfur dissolves in the liquid electrolyte and initiates a reduction down to small-chain polysulfides. Therefore, the

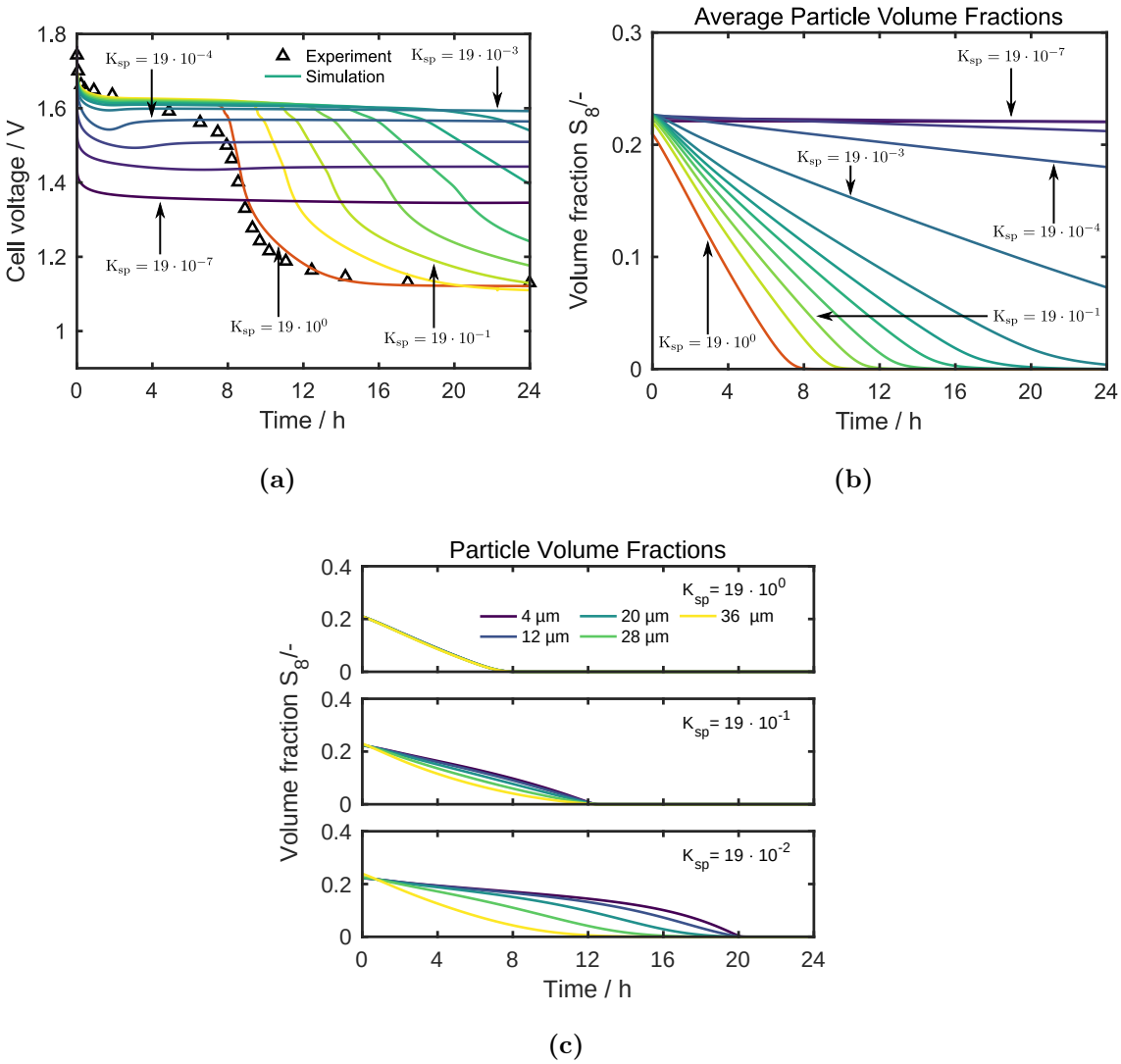

Figure 9: Variation of the solubility of S_8. a) The OCV for different solubilities, where the solid lines represent simulations and the symbols represent experimental data. b) Average volume fraction of solid S_8 within the microscopic pores. c) Spatial volume fraction of solid S_8 along the x-axis from the current collector to separator. In a), the red curve represents the standard parameters for Mg-S and Li-S, respectively. The values of the solubility products are unitless.

kinetics of sulfur dissolution and sulfur solubility are important properties of the system. Alternately, the formation of solid Li2S produces a prominent plateau during the discharge of Li-S batteries, a feature that is not prominent in the discharge curves of Mg-S batteries. Therefore, we also briefly discuss the effect of the MgS formation kinetics on the self-discharge of Mg-S batteries at the end of this section.

$\mathbf{S}_8^{(s)}$ dissolution To address the differences between Li-S and Mg-S batteries, we simulate the effect of varying the sulfur solubility K_{sp} and kinetic factor k_{f}^0 of the $\mathbf{S}_8^{(s)} \rightleftharpoons \mathbf{S}_8^{(l)}$ reaction. The results for a varying kinetic factor k_{f}^0 are shown in Fig. 8 a), where the red curve indicates the simulated OCV with the standard Mg-S parameters and the dashed orange curve indicates the simulated OCV of Mg-S cells with the parameters of the Li-S system. Fig. 8 b) shows the average S_8 volume fraction in the cathode and c) the spatial distribution of solid S_8 within the microscopic pores along the x-axis for selected values of k_{f}^0, respectively. Starting with standard parameters, a decrease in k_{f}^0 causes a smooth transition from the upper to the lower plateau, as indicated by the red arrow in Fig. 8 a). Further decreasing the dissolution kinetics results in a voltage signal similar to that observed in Li-S batteries. Indeed, k_{f}^0 is similar to the value in Li-S battery simulations. In this parameter range, we start to see incomplete dissolution of sulfur within the 24-h rest period. For even slower dissolution kinetics, we observe an immediate drop in cell voltage to a lower plateau. The position of the plateau shifts to a lower cell voltage with decreasing k_{f}^0. All $S_8^{(l)}$ coming from the cathode is immediately reduced to S at the anode. The subsequent reduction of S_4^{2-} to S^{2-} shifts the cell voltage, as indicated by the blue arrow in Fig. 8 a). Moreover, an interesting feature in the cell voltage appears that resembles the nucleation feature in Li-S batteries. The sudden drop of the $S_8^{(l)}$ concentration stops the $S_8^{(l)}$ to S_4^{2-} reduction reaction at the anode. Then, the rapid reduction of S_4^{2-} to S^{2-} leads to an increase in the S^{2-} concentration, as shown in Fig. S4. The rapid change in concentration leads to a nucleation dip in cell voltage according to Eq. 26.

The effect of the solubility of $S_8^{(s)}$ on the self-discharge in Mg-S cells is shown in Fig. 9 a), b), and c). Like a reduction of the frequency factor, the reduction of the solubility first suppresses the two-plateau behavior before causing a sudden drop in cell voltage. However, the mechanism causing this effect is slightly different. On the one hand, the solubility sets the maximum concentration in the liquid electrolyte, which affects the potential through Eq. (12) and causes the slight shift of the voltage in the initial stage of the upper plateau. Moreover, the concentration affects the diffusion of dissolved S_8 from the cathode to the anode. On the other hand, the solubility product also influences the dissolution kinetics, as seen by Eq. (13). Both effects have an impact on the distribution of the concentrations and solid phases in the cell. The effect of the kinetics is discussed in the paragraph above. Here, we focus on the concentration aspect, which causes a qualitatively different distribution of solid sulfur after the 24-h rest period, as indicated in Fig. 9 c). As described above, diffusion limited transport of $S_8^{(l)}$ from the cathode to anode causes a spatial gradient in the $S_8^{(s)}$ solid volume fraction. With decreasing solubility, the concentration gradient driving the diffusion of $S_8^{(l)}$ decreases, and thus, the corresponding flux decreases as well. This effect leads to a pronounced spatial gradient in the $S_8^{(s)}$ volume fraction at low solubility, which contrasts with the simulations with a small frequency factor, where the distribution is always more uniform. Note that the solubility must be two orders of magnitude lower to suppress the formation of the second plateau. Studies in the literature show that the salt indeed influences sulfur solubility.[56] However, this effect is typically less than an order of magnitude in the same solvent system.

The simulations demonstrate the influence of sulfur dissolution on the self-discharge, which shows that the slow dissolution of sulfur can indeed lead to the flat OCV behavior, as seen in the Li-S system. Additional aspects are analyzed in section 4.3.3 with a focus on the anode kinetics.

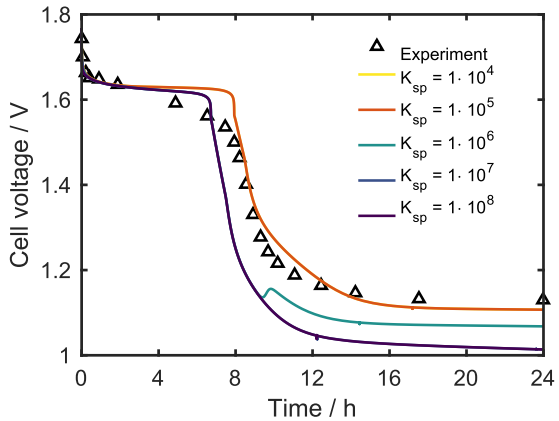

(a)

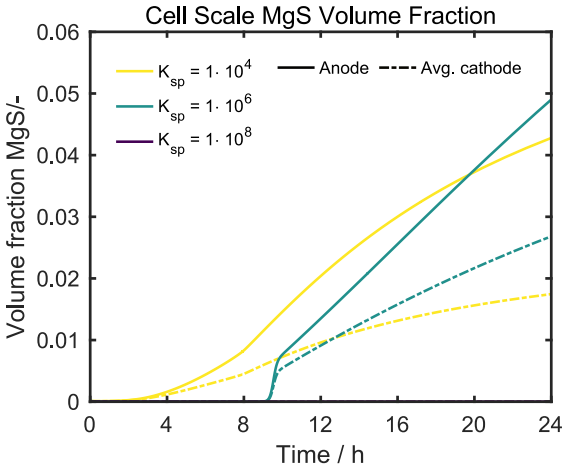

(b)

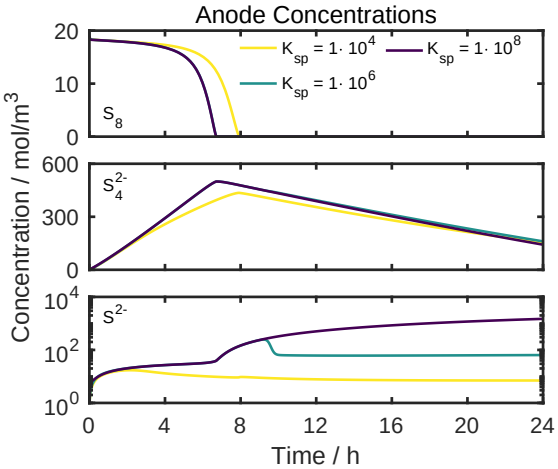

(c)

Figure 10: Analysis of the effect of MgS solubility. a) OCV for different solubilities, where the lines represent simulations and the symbols show experimental data. b) Cathode macropore volume fractions and anode volume fractions of MgS. c) Species concentrations at the anode. The values of the solubility product are unitless.

MgS precipitation There are contradictory results published in the literature regarding the presence of solid discharge products in Mg-S batteries. Therefore, we include this process in our parameter study to qualitatively analyze the effect of MgS precipitation on self-discharge. Fig. 10 shows simulation results assuming different MgS solubilities. a) Shows the OCV for five different solubilities, and b) and c) show the corresponding MgS volume fractions and polysulfide concentrations at the anode, respectively. The symbols in Fig. 10 a) represent experimental data.

At low solubility, we do not observe a significant influence of MgS solubility on the simulated OCV. According to the corresponding distribution of volume fractions, we see almost instantaneous formation of MgS at the anode. At higher MgS solubility, the length of the upper plateau decreases, as shown in Fig. 10 a). By analyzing the MgS volume fractions in b) and the dissolved species concentrations shown in c), it is evident that the precipitation during the upper plateau is suppressed for high solubilities. As a result, the $S_8^{(l)}$ to S_4^{2-} reaction at the anode causes a quick reduction of dissolved $S_8^{(l)}$ and thus also increased dissolution of solid $S_8^{(s)}$. Once $S_8^{(l)}$ is reduced, the reduction of S_4^{2-} to S^{2-} causes an increasing concentration of S^{2-}, as seen in 10 c). At solubility $K_{sp} = 1 \cdot 10^6$ and $K_{sp} = 1 \cdot 10^7$, the concentration of S^{2-} reaches the critical concentration during the simulation time, and the nucleation of MgS causes a dip in cell voltage before the lower plateau. At $K_{sp} = 1 \cdot 10^8$ and above, precipitation of MgS is totally suppressed.

This study shows that increasing MgS solubility enhances the self-discharge. However, the sensitivity of our simulation of this parameter is rather small, indicating that even extremely low solubility is not able to suppress the capacity fade. Moreover, this study does not explain why MgS is not always seen in experiments. We will investigate this topic in our future research.

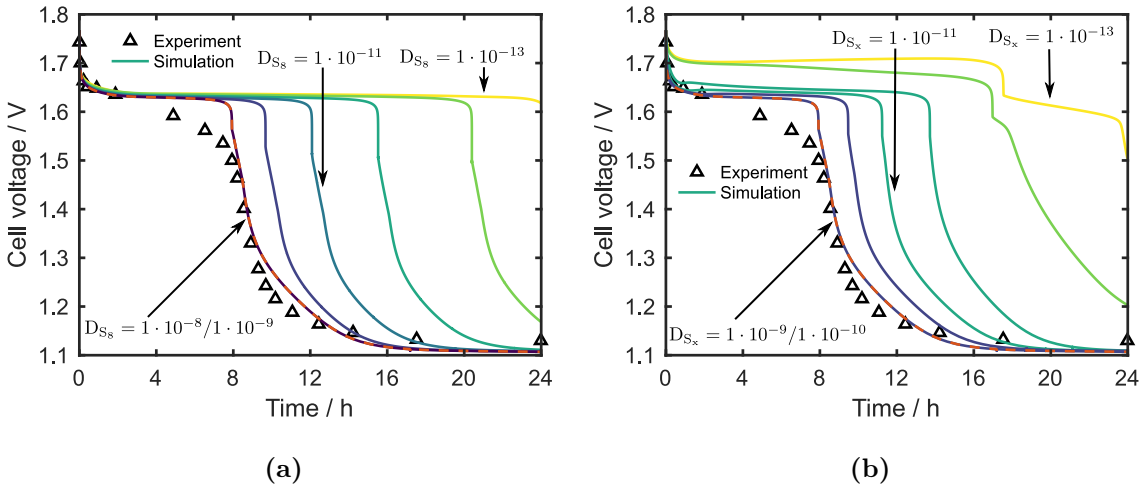

Figure 11: Lines in a) and b) show the simulated OCV for varying mobilities of S_8 and charged polysulfides, respectively. The red curves indicate the standard parameters, and the symbols represent our measurements. The diffusion coefficients are given in m^2/s.

4.3.2 Mobility of dissolved species

In this section, we study the mobility of dissolved sulfur species, which is, according to our sensitivity analysis, another factor controlling the self-discharge of Me-S batteries. First, we investigate the mobility of S_8 given by the diffusion coefficient.

In Section 4.3.1, we observe a considerable effect of sulfur dissolution kinetics on the self-discharge rate, and we expect similar trends due to the mobility of S_8 To limit the number of simulations, the second case that we investigate focuses on the general mobility of charged polysulfide species. Fig. 11 a) shows simulation results of an Mg-S cell with a varying S_8 diffusion coefficient. Fig. 11 b) shows OCVs where only the diffusion coefficient of the polysulfide species S_4^{2-} and S^{2-} is varied. The first information that we can extract from Fig. 11 a) and b) is that increasing diffusion coefficients do not affect the OCV. Moreover, considering the lower conductivity of the Mg salt,[15] we expect a lower mobility of dissolved species in the Mg electrolyte compared to the Li system. Therefore, we conclude that the mobility of polysulfides is most likely not causing accelerated self-discharge of MgS batteries. Still, it is interesting that reduced mobility can reduce the self-discharge of Mg-S batteries, which provides useful information for mitigation strategies of the polysulfide-shuttle. For

instance, a reduction of the mobility of all polysulfide species mimics the effect of an ideal diffusion barrier and corresponds to the second case displayed in Fig. 11 b).

By gradually reducing the diffusion coefficient in our simulations, we indeed see OCV curves that are similar to those of Li-S batteries. However, the diffusion coefficients need to be lower than 10^{-13} m^2/s to avoid a drop in cell voltage to the second plateau, which corresponds to a change in the characteristic diffusion time scale from a few minutes up to days. Under these conditions, we estimate ohmic losses in the separator of up to 100 mV for a 0.1 C discharge. For the development of new cell concepts for Mg-S batteries, a general reduction of the mobility of dissolved species is, therefore, not suitable to prevent self-discharge without compromising battery performance.

4.3.3 Anode electrochemical kinetics

The side reactions on the anode surface are key to understanding the self-discharge process. In the following section, we will investigate the influence of the anode kinetics on the self-discharge rate. Fig. 12 shows the simulation results for varying frequency factors of the $S_8^{(l)}$ to S_4^{2-} reaction, and Fig. 13 shows the results for varying frequency factors of the S_4^{2-} to S^{2-} reaction. In both cases, we compare the OCV curves (graph a)), concentrations (graph b)), and volume fractions on at the particle (graph c)) and cell levels (graph d)). OCV curves with standard parameters and the corresponding experimental data are given by red solid lines and black symbols, respectively. Figs. 12 and 13 a) show that both parameters have a similar effect on the OCV curve of the battery. A lower frequency factor increases in both cases the length of the upper plateau in both cases, and increasing frequency factors reduce the length of the upper plateau. This correlation can be explained by analyzing the reduction mechanism and its connection to species concentration in the electrolyte. For example, the fast reduction of S_4^{2-} to S^{2-} reduces the S concentration, which in turn, affects the reaction rate of the $S_8^{(l)}$ to S_4^{2-} reduction. Generally, the high sensitivity of the kinetic parameters at the anode is due to the large overpotentials of the polysulfide reactions. The difference

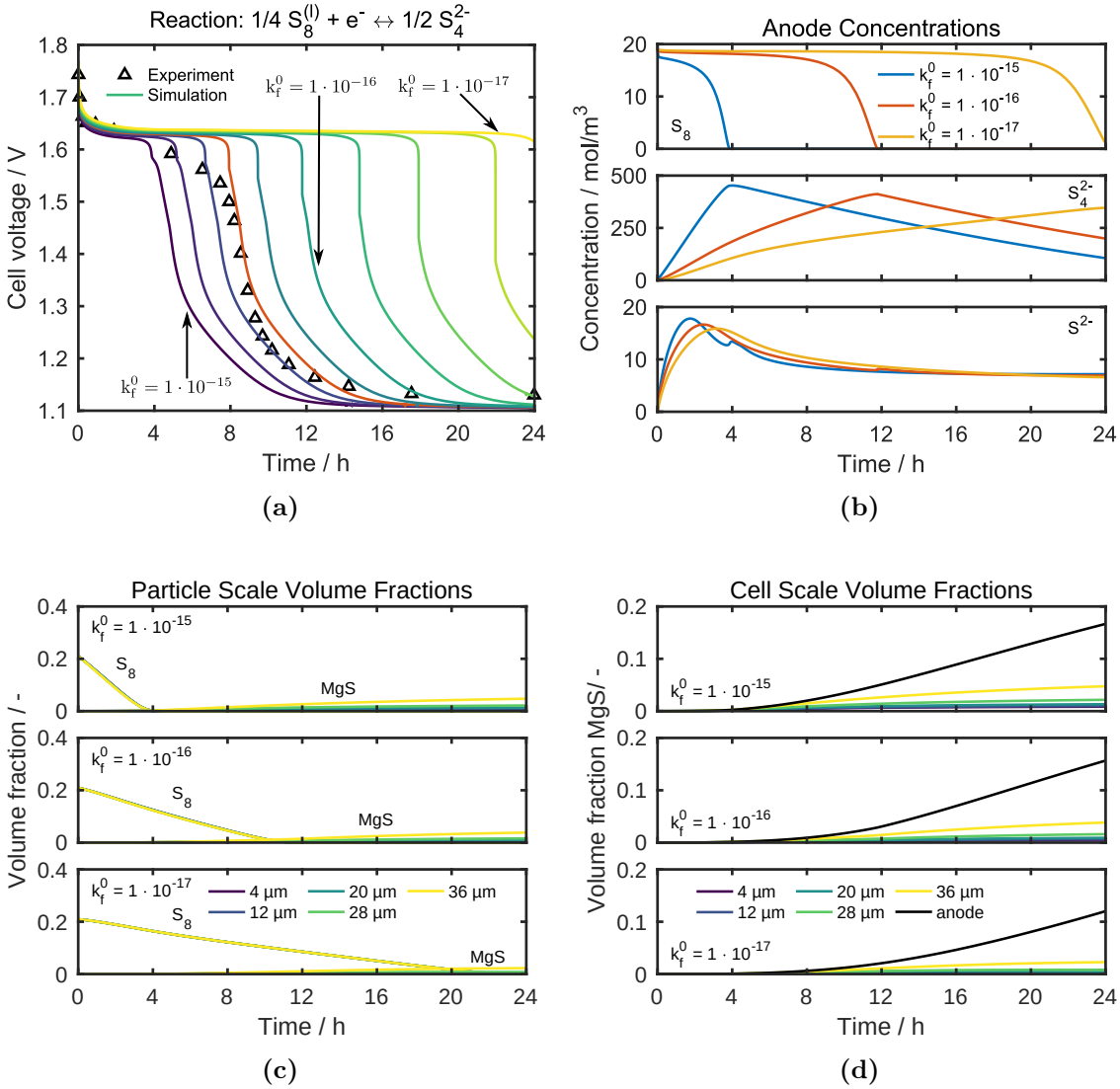

Figure 12: Effect of varying frequency factors of the $S_8^{(l)}$ to S_4^{2-} reduction reaction at the anode. a) The OCV for varying frequency factors. The red curve indicates the standard parameters, and the symbols represent experimental data. b) The anode concentrations of polysulfides. c) Spatial micropore volume fraction along the x-axis from the current collector to separator. d) Anode volume fraction and spatial macropore volume fraction along the x-axis from the current collector to separator. The frequency factors are given in mol/m^{2}s.

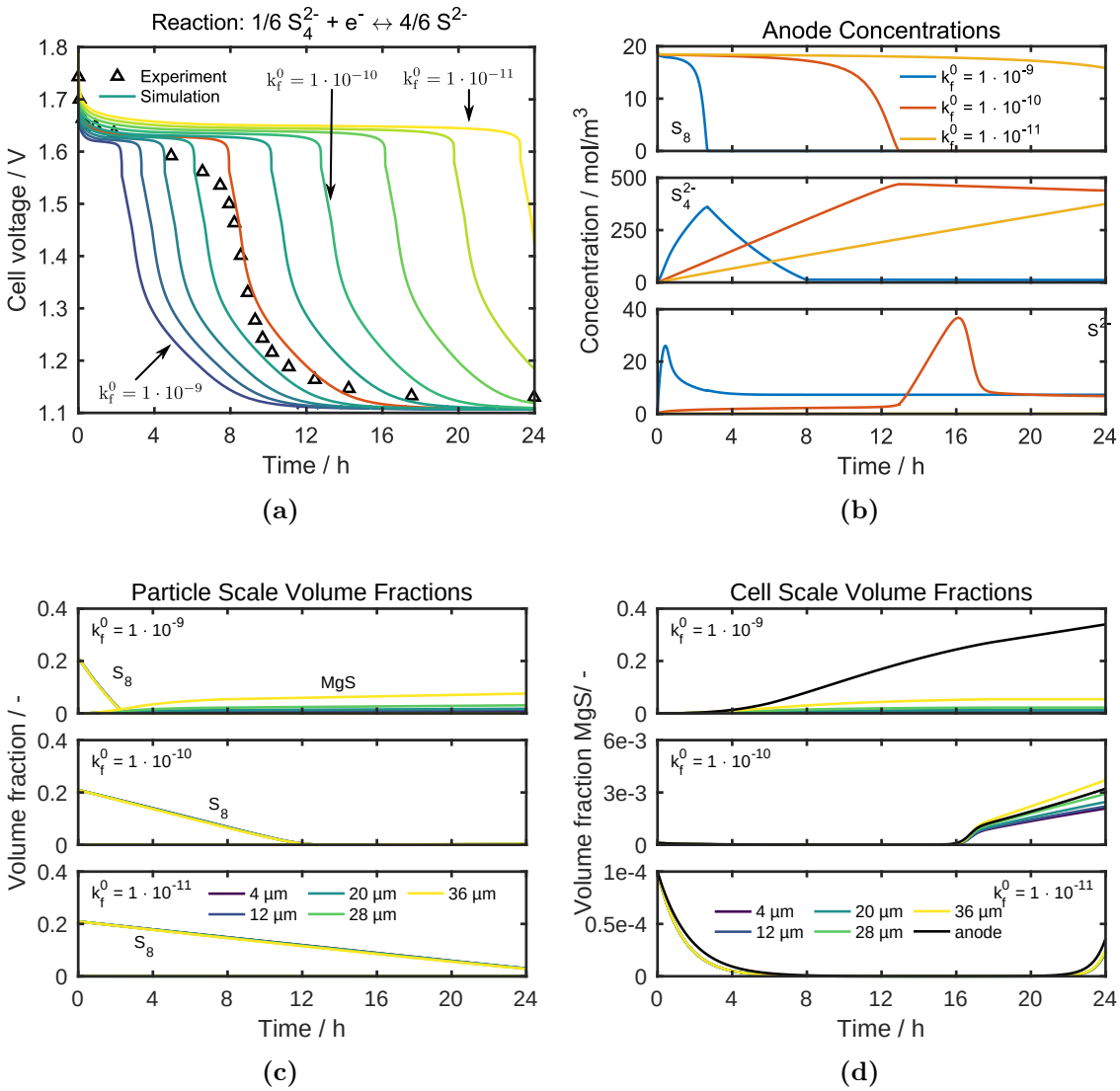

Figure 13: Effect of varying frequency factors of the S_4^{2-} to S^{2-} reduction reaction at the anode. a) The OCV for varying frequency factors. The red curve indicates the standard parameters, and the symbols represent experimental data. b) The anode concentrations of polysulfides. c) Spatial micropore volume fraction along the x-axis from the current collector to separator. d) Anode volume fraction and spatial macropore volume fraction along the x-axis from the current collector to separator. The frequency factors are given in mol/m^{2}s.

in the equilibrium potentials of the sulfur reduction reactions and the equilibrium potential of the plating/stripping reaction exceeds 1 V. The corresponding substantial difference in electrochemical potential drives the fast quick reduction of polysulfides on the anode surface. Therefore, OCV curves are extremely sensitive to even small changes in the frequency factor. Figs. 12 and 13 b) througho d) show the temporal evolution of the concentrations and volume fractions in the battery for different kinetic parameters. Considering the similar trends in the OCV curves, it is not surprising that both parameters result in similar distributions of concentrations and volume fractions. However, there is one distinct difference between both cases. Reduction The reduction of the frequency factor of the $S_8^{(l)}$ to S_4^{2-} reaction at the anode shows has less impact on the MgS formation compared to the reduction of the frequency factor of the S_4^{2-} to S^{2-} reaction. The reduction kinetics of long-chain polysulfides have a minor impact on MgS formation, as shown in Fig. 12 d). Slower The slower reduction kinetics of short polysulfides, in turn, reduce the formation of MgS significantly. This is due to a generally low concentration of S^{2-} in the electrolyte during the 24 h under open- circuit conditions. Finally, we compare the standard kinetic parameters of the side reactions on the Li and Mg metal surfaces, which we determined by fitting the experimental data. The values of these parameters differ by orders of magnitude, which indicates that the difference in the self-discharge rate probably arises from the side reactions at the anode. One explanation causing for this difference might be the formation of a solid electrolyte interphase (SEI), which passivates the Li metal anode in Li-S batteries.[7] A similar protective film seems not to not form in the Mg-S batteries investigated in this work. This finding is in line with similar studies in the literature, and we will have take a closer look into this interesting topic in our future work. Interphases which that passivate the Mg surface and still conduct bivalent Mg ions are not reported in the literature, yet.[57–59] Therefore, we think that an artificial SEI on the Mg surface preventing the reduction of polysulfides might be a promising concept to reduce the self-discharge and polysulfide-shuttle in Mg-S batteries. Note, that we use in our model only two representative reactions to reproduce the experimental data. More

electrochemical steps are likely, which could change the qualitative conclusions drawn above. Still, our simulations show, that the reduction of polysulfides species at the anode is most likely the key process causing a very rapid self-discharge of the battery.

5 Conclusion

Magnesium-sulfur batteries promise significant improvements in energy density. Moreover, the active materials are cheap and abundant, which makes Mg-S batteries interesting for several applications, including electric vehicles. However, in our experiments, we observe a rapid self-discharge, which is even faster than that in Li-S batteries with a similar cell design. To support the development of improved Mg-S batteries, we want to take advantage of the similarities between Mg-S and Li-S batteries. Therefore, we developed a simulation framework for Me-S batteries. The self-discharge is modeled by including a shuttle of polysulfide species between the cathode and anode, as well as the side reactions of polysulfide species on the anode surface. The model parameters of Li-S and Mg-S batteries are determined from the literature and by fitting the experimental data. Our simulations reproduce OCV curves and self-discharge rates for both systems, which is the basis for parameter studies. First, a sensitivity analysis is performed to identify the key processes causing the rapid self-discharge of Mg-S batteries during storage under open-circuit conditions. Several parameters have a high impact on the simulation results. The most prominent ones are the mobility, solubility, and dissolution kinetics of sulfur species in the liquid electrolyte and the kinetics of the side reactions on the anode surface. Our subsequent parameter studies indicate that the extremely fast kinetics of the side reactions on the Mg surface are likely responsible for the rapid self-discharge. These side reactions are connected to the polysulfide shuttle. Therefore, we also use our parameter studies to evaluate strategies to mitigate the shuttle effect. Low solubilities or dissolution kinetics reduce the self-discharge but, at the same time, also adversely affect the power density of the battery. Similarly, the lower mobility of the

dissolved species in the separator reduces the self-discharge but also increases ohmic losses. Therefore, we believe an artificial SEI between the Mg anode and separator that reduces side reactions on the metal surface is a promising strategy to mitigate the self-discharge and other negative effects of the polysulfide shuttle. Our study demonstrates that even in a geometrically identical cell setup, there are distinct differences between Li-S and Mg-S batteries. Therefore, intensive research on new electrode materials and electrolyte systems is needed to improve the performance, as well as our understanding, of Mg-S batteries. Our framework is an additional tool that helps to interpret and guide the further development of Mg-S and Li-S batteries.

Acknowledgement

This work was supported by the Federal Ministry for Education and Research of Germany (Bundesministerium für Bildung und Forschung, BMBF) within the project "Mags"(03XP0032A). This work contributes to the research performed at CELEST (Center for Electrochemical Energy Storage Ulm-Karlsruhe).

Supporting Information Available

The following files are available free of charge.

- Supporting Information.pdf: Li-S and Mg-S OCV comparison, additional OCV measurements, Li-S simulations with higher sulfur utilization, anode polysulfide concentrations for varying S8 dissolution kinetics, variation of cathode reduction kinetics, cathode concentrations for varying anode reduction kinetics, detailed discussion if of species mobility variation.

References

(1) Peled, E.; Gorenshtein, A.; Segal, M.; Sternberg, Y. Rechargeable lithium-sulfur battery. *Journal of Power Sources* **2003**, *26*, 269–271.

(2) Bruce, P. G.; Freunberger, S. A.; Hardwick, L. J.; Tarascon, J. M. LigO2and LigS batteries with high energy storage. *Nature Materials* **2012**, *11*, 19–29.

(3) Zhao-Karger, Z.; Zhao, X.; Diemant, T.; Behm, R. J.; Fichtner, M. Performance Improvement of Magnesium Sulfur Batteries with Modified Non-Nucleophilic Electrolytes. *Advanced Energy Materials* **2015**, *5*, 1401155.

(4) Bresser, D.; Passerini, S.; Scrosati, B. Recent progress and remaining challenges in sulfur-based lithium secondary batteries - a review. *Chemical Communications* **2013**, *49*, 10545–10562.

(5) Zhang, S. S. Liquid electrolyte lithium/sulfur battery: Fundamental chemistry, problems, and solutions. *Journal of Power Sources* **2013**, *231*, 153–162.

(6) Zhu, Y.; Wang, S.; Miao, Z.; Liu, Y.; Chou, S. L. Novel Non-Carbon Sulfur Hosts Based on Strong Chemisorption for Lithium-Sulfur Batteries. *Small* **2018**, *14*, 1–21.

(7) Wang, A.; Kadam, S.; Li, H.; Shi, S.; Qi, Y. Review on modeling of the anode solid electrolyte interphase (SEI) for lithium-ion batteries. *npj Computational Materials* **2018**, *4*.

(8) Wild, M.; O'Neill, L.; Zhang, T.; Purkayastha, R.; Minton, G.; Marinescu, M.; Offer, G. J. Lithium sulfur batteries, a mechanistic review. *Energy and Environmental Science* **2015**, *8*, 3477–3494.

(9) Barchasz, C.; Leprêtre, J. C.; Alloin, F.; Patoux, S. New insights into the limiting parameters of the Li/S rechargeable cell. *Journal of Power Sources* **2012**, *199*, 322–330.

(10) Tarascon, J. M.; Armand, M. Issues and challenges facing rechargeable lithium batteries. *Nature* **2001**, *414*, 359–367.

(11) Jäckle, M.; Groß, A. Microscopic properties of lithium, sodium, and magnesium battery anode materials related to possible dendrite growth. *Journal of Chemical Physics* **2014**, *141*.

(12) Ling, C.; Banerjee, D.; Matsui, M. Study of the electrochemical deposition of Mg in the atomic level: Why it prefers the non-dendritic morphology. *Electrochimica Acta* **2012**, *76*, 270–274.

(13) Aurbach, D.; Schechter, A.; Gofer, Y. Prototype systems for rechargeable magnesium batteries. *Nature* **2000**, *407*, 10–14.

(14) Kim, H. S.; Arthur, T. S.; Allred, G. D.; Zajicek, J.; Newman, J. G.; Rodnyansky, A. E.; Oliver, A. G.; Boggess, W. C.; Muldoon, J. Structure and compatibility of a magnesium electrolyte with a sulphur cathode. *Nature Communications* **2011**, *2*, 426–427.

(15) Zhao-Karger, Z.; Fichtner, M. Magnesium-sulfur battery: its beginning and recent progress. *MRS Communications* **2017**, *7*, 770–784.

(16) Zhao-Karger, Z.; Liu, R.; Dai, W.; Li, Z.; Diemant, T.; Vinayan, B. P.; Bonatto Minella, C.; Yu, X.; Manthiram, A.; Behm, R. J.; Ruben, M.; Fichtner, M. Toward Highly Reversible Magnesium-Sulfur Batteries with Efficient and Practical Mg[B(hfip)4]2 Electrolyte. *ACS Energy Letters* **2018**, *3*, 2005–2013.

(17) Zhao-Karger, Z.; Fichtner, M. Beyond Intercalation Chemistry for Rechargeable Mg Batteries: A Short Review and Perspective. *Frontiers in Chemistry* **2019**, *6*, 656.

(18) Vinayan, B. P.; Zhao-Karger, Z.; Diemant, T.; Chakravadhanula, V. S. K.; Schwarzburger, N. I.; Cambaz, M. A.; Behm, R. J.; Kübel, C.; Fichtner, M. Performance

study of magnesium-sulfur battery using a graphene based sulfur composite cathode electrode and a non-nucleophilic Mg electrolyte. *Nanoscale* **2016**, *8*, 3296–3306.

(19) Robba, A.; Vizintin, A.; Bitenc, J.; Mali, G.; Arčon, I.; Kavčič, M.; Žitnik, M.; Bučar, K.; Aquilanti, G.; Martineau-Corcos, C.; Randon-Vitanova, A.; Dominko, R. Mechanistic Study of Magnesium-Sulfur Batteries. *Chemistry of Materials* **2017**, *29*, 9555–9564.

(20) Gao, T.; Ji, X.; Hou, S.; Fan, X.; Li, X.; Yang, C.; Han, F.; Wang, F.; Jiang, J.; Xu, K.; Wang, C. Thermodynamics and Kinetics of Sulfur Cathode during Discharge in MgTFSI 2 -DME Electrolyte. *Advanced Materials* **2017**, *30*, 1704313.

(21) Yu, X.; Manthiram, A. Performance Enhancement and Mechanistic Studies of Magnesium-Sulfur Cells with an Advanced Cathode Structure. *ACS Energy Letters* **2016**, *1*, 431–437.

(22) Tutusaus, O.; Mohtadi, R.; Singh, N.; Arthur, T. S.; Mizuno, F. Study of Electrochemical Phenomena Observed at the Mg Metal/Electrolyte Interface. *ACS Energy Letters* **2017**, *2*, 224–229.

(23) Mikhaylik, Y. V.; Akridge, J. R. Polysulfide Shuttle Study in the Li/S Battery System. *Journal of The Electrochemical Society* **2004**, *151*, A1969.

(24) Kumaresan, K.; Mikhaylik, Y.; White, R. E. A Mathematical Model for a Lithium-Sulfur Cell. *Journal of The Electrochemical Society* **2008**, *155*, A576.

(25) Ghaznavi, M.; Chen, P. Sensitivity analysis of a mathematical model of lithium-sulfur cells part I: Applied discharge current and cathode conductivity. *Journal of Power Sources* **2014**, *257*, 394–401.

(26) Ghaznavi, M.; Chen, P. Sensitivity analysis of a mathematical model of lithium-sulfur

cells: Part II: Precipitation reaction kinetics and sulfur content. *Journal of Power Sources* **2014**, *257*, 402–411.

(27) Ghaznavi, M.; Chen, P. Analysis of a Mathematical Model of Lithium-Sulfur Cells Part III: Electrochemical Reaction Kinetics, Transport Properties and Charging. *Electrochimica Acta* **2014**, *137*, 575–585.

(28) Fronczek, D. N.; Bessler, W. G. Insight into lithium-sulfur batteries: Elementary kinetic modeling and impedance simulation. *Journal of Power Sources* **2013**, *244*, 183–188.

(29) Hofmann, A. F.; Fronczek, D. N.; Bessler, W. G. Mechanistic modeling of polysulfide shuttle and capacity loss in lithium-sulfur batteries. *Journal of Power Sources* **2014**, *259*, 300–310.

(30) Zhang, T.; Marinescu, M.; O'Neill, L.; Wild, M.; Offer, G. Modeling the voltage loss mechanisms in lithium-sulfur cells: The importance of electrolyte resistance and precipitation kinetics. *Physical Chemistry Chemical Physics* **2015**, *17*, 22581–22586.

(31) Danner, T.; Zhu, G.; Hofmann, A. F.; Latz, A. Modeling of nano-structured cathodes for improved lithium-sulfur batteries. *Electrochimica Acta* **2015**, *184*, 124–133.

(32) Thangavel, V.; Xue, K.-H.; Mammeri, Y.; Quiroga, M.; Mastouri, A.; Guéry, C.; Johansson, P.; Morcrette, M.; Franco, A. A. A Microstructurally Resolved Model for Li-S Batteries Assessing the Impact of the Cathode Design on the Discharge Performance. *Journal of The Electrochemical Society* **2016**, *163*, A2817–A2829.

(33) Yin, Y.; Franco, A. A. Unraveling the Operation Mechanisms of Lithium Sulfur Batteries with Ultramicroporous Carbons. *ACS Applied Energy Materials* **2018**, *1*, 5816–5821.

(34) Sleightholme, A. E. S.; Vardar, G.; Chadwick, A. F.; Siegel, D. J.; DeWitt, S.; Thornton, K.; Monroe, C. W. Computational Model of Magnesium Deposition and Dissolution

for Property Determination via Cyclic Voltammetry. *Journal of The Electrochemical Society* **2016**, *163*, A1813–A1821.

(35) Mikhaylik, Y. V. Electrolytes for Lithium Sulfur Cells. U.S. Patent 7,352,680, 2008.

(36) Zhou, K.; Fan, X. J.; Wei, X. F.; Liu, J. H. The strategies of advanced cathode composites for lithium-sulfur batteries. *Science China Technological Sciences* **2017**, *60*, 175–185.

(37) Lu, Y. C.; He, Q.; Gasteiger, H. A. Probing the lithium-sulfur redox reactions: A rotating-ring disk electrode study. *Journal of Physical Chemistry C* **2014**, *118*, 5733–5741.

(38) Conder, J.; Villevieille, C.; Trabesinger, S.; Novák, P.; Gubler, L.; Bouchet, R. Electrochemical impedance spectroscopy of a Li-S battery: Part 2. Influence of separator chemistry on the lithium electrode/electrolyte interface. *Electrochimica Acta* **2017**, *255*, 379–390.

(39) Conder, J.; Villevieille, C.; Trabesinger, S.; Novák, P.; Gubler, L.; Bouchet, R. Electrochemical impedance spectroscopy of a Li-S battery: Part 1. Influence of the electrode and electrolyte compositions on the impedance of symmetric cells. *Electrochimica Acta* **2017**, *244*, 61–68.

(40) Hintz, F.; Krewer, U.; Sch, P. Electrochemical analysis of the reaction mechanism of sulfur reduction as a function of state of charge. *Electrochim Acta* **2019**, *295*, 926–933.

(41) Häcker, J.; Danner, C.; Sievert, B.; Biswas, I.; Zhao-Karger, Z.; Wagner, N.; Friedrich, K. A. Investigation of Magnesium–Sulfur Batteries using Electrochemical Impedance Spectroscopy. *Electrochimica Acta* **2020**, *338*, 135787.

(42) Bieker, G.; Diddens, D.; Kolek, M.; Borodin, O.; Winter, M.; Bieker, P.; Jalkanen, K.

Cation-Dependent Electrochemistry of Polysulfides in Lithium and Magnesium Electrolyte Solutions. *The Journal of Physical Chemistry C* **2018**, *122*, 21770–21783.

(43) Xu, Y.; Ye, Y.; Zhao, S.; Feng, J.; Li, J.; Chen, H.; Yang, A.; Shi, F.; Jia, L.; Wu, Y.; Yu, X.; Glans-Suzuki, P.-A.; Cui, Y.; Guo, J.; Zhang, Y. In Situ X-ray Absorption Spectroscopic Investigation of the Capacity Degradation Mechanism in Mg/S Batteries . *Nano Letters* **2019**, *19*, 2928–2934.

(44) Bazant, M. Z. Theory of chemical kinetics and charge transfer based on nonequilibrium thermodynamics. *Accounts of Chemical Research* **2013**, *46*, 1144–1160.

(45) Latz, A.; Zausch, J. Thermodynamic derivation of a Butler-Volmer model for intercalation in Li-ion batteries. *Electrochimica Acta* **2013**, *110*, 358–362.

(46) Andrei, P.; Shen, C.; Zheng, J. P. Theoretical and experimental analysis of precipitation and solubility effects in lithium-sulfur batteries. *Electrochimica Acta* **2018**, *284*, 469–484.

(47) Ren, Y. X.; Zhao, T. S.; Liu, M.; Tan, P.; Zeng, Y. K. Modeling of lithium-sulfur batteries incorporating the effect of Li2S precipitation. *Journal of Power Sources* **2016**, *336*, 115–125.

(48) Horstmann, B.; Danner, T.; Bessler, W. G. Precipitation in aqueous lithium-oxygen batteries: A model-based analysis. *Energy and Environmental Science* **2013**, *6*, 1299–1314.

(49) Su, L.; Ferrandon, M.; Barton, J. L.; de la Rosa, N. U.; Vaughey, J. T.; Brushett, F. R. An investigation of 2,5-di-tertbutyl-1,4-bis(methoxyethoxy)benzene in ether-based electrolytes. *Electrochimica Acta* **2017**, *246*, 251–258.

(50) Hu, J. J.; Long, G. K.; Liu, S.; Li, G. R.; Gao, X. P. A LiFSI-LiTFSI binary-salt

electrolyte to achieve high capacity and cycle stability for a Li-S battery. *Chemical Communications* **2014**, *50*, 14647–14650.

(51) Park, M. S.; Ma, S. B.; Lee, D. J.; Im, D.; Doo, S. G.; Yamamoto, O. A highly reversible lithium metal anode. *Scientific Reports* **2014**, *4*, 1–8.

(52) Zhao-Karger, Z.; Zhao, X.; Fuhr, O.; Fichtner, M. Bisamide based non-nucleophilic electrolytes for rechargeable magnesium batteries. *RSC Advances* **2013**, *3*, 16330–16335.

(53) Hollemann, A. F.; Wiberg, E. *Lehrbuch der anorganischen Chemie*, 101st ed.; Walter de Gruyter: Berlin, 1995.

(54) Lide, D. R. *CRC handbook of chemistry and physics*, 87th ed.; CRC press, 2006.

(55) Shen, C.; Xie, J.; Zhang, M.; Andrei, P.; Hendrickson, M.; Plichta, E. J.; Zheng, J. P. Self-Discharge Behavior of Lithium-Sulfur Batteries at Different Electrolyte/Sulfur Ratios. *Journal of The Electrochemical Society* **2019**, *166*, A5287–A5294.

(56) Jeschke, S.; Johansson, P. Predicting the Solubility of Sulfur: A COSMO-RS-Based Approach to Investigate Electrolytes for Li-S Batteries. *Chemistry - A European Journal* **2017**, *23*, 9130–9136.

(57) Salama, M.; Attias, R.; Hirsch, B.; Yemini, R.; Gofer, Y.; Noked, M.; Aurbach, D. On the Feasibility of Practical Mg–S Batteries: Practical Limitations Associated with Metallic Magnesium Anodes. *ACS Applied Materials & Interfaces* **2018**, *10*, 36910–36917, PMID: 30295459.

(58) Yoo, H. D.; Shterenberg, I.; Gofer, Y.; Gershinsky, G.; Pour, N.; Aurbach, D. Mg rechargeable batteries: an on-going challenge. *Energy Environ. Sci.* **2013**, *6*, 2265–2279.

(59) Aurbach, D.; Weissman, I.; Gofer, Y.; Levi, E. Nonaqueous magnesium electrochemistry and its application in secondary batteries. *The Chemical Record* **2003**, *3*, 61–73.

Graphical TOC Entry